

Central Lancashire Online Knowledge (CLoK)

Title	HD 60435: The star that stopped pulsating
Type	Article
URL	https://clok.uclan.ac.uk/id/eprint/53920/
DOI	https://doi.org/10.1093/mnras/stae2708
Date	2024
Citation	Kurtz, Donald Wayne, Handler, Gerald, Holdsworth, Daniel Luke orcid iconORCID: 0000-0003-2002-896X, Cunha, M. S., Saio, Hideyuki, Medupe, Thebe, Murphy, Simon, Kruger, Joachim, Brunsden, Emily et al (2024) HD 60435: The star that stopped pulsating. Monthly Notices of the Royal Astronomical Society, 536 (3). pp. 2103-2126. ISSN 0035-8711
Creators	Kurtz, Donald Wayne, Handler, Gerald, Holdsworth, Daniel Luke, Cunha, M. S., Saio, Hideyuki, Medupe, Thebe, Murphy, Simon, Kruger, Joachim, Brunsden, Emily, Antoci, Victoria, Hey, Daniel, Shitrit, Noi and Matthews, Jaymie

It is advisable to refer to the publisher's version if you intend to cite from the work. https://doi.org/10.1093/mnras/stae2708

For information about Research at UCLan please go to http://www.uclan.ac.uk/research/

All outputs in CLoK are protected by Intellectual Property Rights law, including Copyright law. Copyright, IPR and Moral Rights for the works on this site are retained by the individual authors and/or other copyright owners. Terms and conditions for use of this material are defined in the http://clok.uclan.ac.uk/policies/

Advance Access publication 2024 December 10



Downloaded from https://academic.oup.com/mnras/article/536/3/2103/7920801 by University of Central Lancashire user on 07 January 2025

HD 60435: the star that stopped pulsating

Donald W. Kurtz[©], ^{1,2}* Gerald Handler, ³ Daniel L. Holdsworth [©], ^{2,4,5} Margarida S. Cunha [©], ⁶ Hideyuki Saio, ⁷ Thebe Medupe, ¹ Simon J. Murphy [©], ⁸ Joachim Krüger, ⁸ E. Brunsden, ⁵ Victoria Antoci, ⁹ Daniel R. Hey, ¹⁰ Noi Shitrit ¹¹ and Jaymie M. Matthews ¹²

Accepted 2024 December 4. Received 2024 November 23; in original form 2024 October 4

ABSTRACT

HD 60435 is a well known rapidly oscillating (roAp) Ap star with a series of alternating even and odd degree modes, making it a prime asteroseismic target. It is also an oblique pulsator with rotational inclination, i, and magnetic/pulsation obliquity, β , such that both magnetic/pulsation poles are viewed over the rotation period, $P_{\text{rot}} = 7.679696 \, \text{d}$, determined from rotational light variations. While some roAp stars have stable pulsation mode amplitudes over decades, HD 60435 is known to have amplitude variations on time-scales as short as 1 d. We show from 5 yr of *TESS* observations that there is strong amplitude modulation on this short time-scale with possible mode interactions. Most remarkably, HD 60435 stopped pulsating during the time span of the *TESS* observations. This is the first time that any pulsating star has been observed to cease pulsating entirely. That has implications for mode interaction, excitation and damping, and is relevant to the problem of why only some stars in many pulsation instability strips pulsate, while others do not. During a 24.45-d time span of the *TESS* data when there was mode stability for a dipole mode and a quadrupole mode, the oblique pulsator model constrained i and β , which we used to model those modes with a magnetic pulsation model from which we determined a polar field strength of 4 kG, in good agreement with a known magnetic measurement. We modelled the frequency separations showing that they can constrain the global metallicity, something that is not possible from spectroscopy of the highly peculiar Ap atmosphere.

Key words: asteroseismology – stars: chemically peculiar – stars: individual: (HD 60435) – stars: oscillations.

1 INTRODUCTION

Stellar pulsation is ubiquitous across the Hertzsprung–Russell (HR) diagram, occurring in many classes of stars. In recent years precise astrophysical inference of stellar structure has become possible through asteroseismology (e.g. Aerts, Christensen-Dalsgaard & Kurtz 2010; Aerts 2021; Kurtz 2022). A given star may pulsate as different kinds of variables during its lifetime, as it evolves into and out of various pulsational instability strips or regions in the HR diagram (e.g. see figs 1 of Aerts 2021; Kurtz 2022). Those regions are defined by boundaries in effective temperature and luminosity that depend on a

competition between pulsational driving in certain layers of the star and damping throughout the star.

For example, a 5-M $_{\odot}$ star may begin life on the main sequence as a slowly pulsating B (SPB) star, move out of the SPB instability strip and stop pulsating, only then to evolve through the Cepheid instability strip where it becomes a δ Cep star (Cepheid), evolve out of that instability strip with Cepheid pulsation stopping, then become a red giant where it becomes a stochastic pulsator and even a Mira variable at various stages. After shedding much of its mass in winds and as a planetary nebula, the typically 0.6-M_{\odot} remnant core then evolves through several instability strips as a DOV, DBV, and DAV white dwarf, crossing regions of stability along the way. Stars of other masses can pass through other instability zones.

Thus, the pulsating stars that are the subjects of asteroseismology have various eigenmodes excited to observable amplitudes as they

¹Centre for Space Research, North-West University, Dr Albert Luthuli Drive, Mahikeng 2735, South Africa

² Jeremiah Horrocks Institute, University of Central Lancashire, Preston PR1 2HE, UK

³Nicolaus Copernicus Astronomical Center, Polish Academy of Sciences, ul. Bartycka 18, 00-716 Warszawa, Poland

⁴South African Astronomical Observatory, PO Box 9, Observatory 7935, Cape Town, South Africa

⁵School of Physics, Engineering and Technology, University of York, Heslington, York YO10 5DD, UK

⁶Instituto de Astrofísica e Ciências do Espaço, Universidade do Porto CAUP, Rua das Estrelas, P-PT4150-762 Porto, Portugal

⁷Astronomical Institute, Graduate School of Science, Tohoku University, Sendai 980-8578, Japan

⁸Centre for Astrophysics, University of Southern Queensland, Toowoomba QLD 4350, Australia

⁹DTU Space, Technical University of Denmark, Elektrovej 327, Kgs. Lyngby 2800, Denmark

¹⁰Institute for Astronomy, University of Hawai'i, Honolulu, HI 96822, USA

¹¹The School of Physics and Astronomy, Tel Aviv University, Tel Aviv 69978, Israel

¹²Department of Physics and Astronomy, University of British Columbia, 6224 Agricultural Road, Vancouver BC V6T 1Z1, Canada

^{*} E-mail: kurtzdw@gmail.com

evolve into instability strips, then extinguished by the dominance of damping as they evolve out at various stages in their evolutionary lives. There is considerable theoretical understanding of pulsation driving mechanisms for the various classes. This is usually the κ -mechanism operating in H, He, or Fe ionization zones for hotter stars and stochastic driving for the cooler stars (see Aerts et al. 2010, section 3.7, for discussion of these mechanisms). But theoretically predicting pulsation amplitude, or explaining observed amplitude in a particular star remains a complex and unsolved problem.

Some stars within a particular instability region may pulsate while others do not; some may have high amplitude while others low amplitude, some may have many eigenmodes excited, while others only one or a few. The problem of mode selection is also complex and unsolved. It is clear that mode excitation and selection are finely tuned to many fundamental parameters, such as $T_{\rm eff}$, $\log g$, metallicity, magnetic field, rotation, binarity, and tides from companions, but our understanding of how these parameters govern observed mode amplitude is weak.

Thus it is of interest when pulsation modes in a star are observed to change amplitude, to appear or disappear, on a human time-scale. This is much shorter than the usual evolutionary time-scales we model. The observations of mode amplitude growth and decay indicate energy exchange among modes – mode interaction – or pulsational energy gains or losses to the driving and damping layers in the star. When a new mode is observed to appear, or a known mode is observed to disappear, this has the potential to provide information on possibly small changes in a star's structure. These amplitude changes, along with frequency changes, can provide detailed understanding of changes in a star on a human time-scale. Such short time-scale changes in stellar structure may be far less smooth than the long time-scale evolution tracks we typically produce with models.

Pulsation amplitude and frequency changes in δ Sct stars are well documented, beginning with 40 yr of pioneering work on 4 CVn (e.g. Breger 2000; Breger et al. 2017). Murphy et al. (2012) showed that three pulsation modes in the δ Sct star KIC 3429637 had linear changes in their pulsation amplitudes over a 2-yr time-span, suggesting evolutionary changes. Bowman et al. (2016) studied 983 δ Sct stars with Kepler main-mission data showing how pulsation amplitude and phase varied over the 4-yr data set for some modes, while others remained at constant amplitude. They showed that the amplitude variations were secular, and not the result of beating among unresolved modes. A spectacular case was found in the δ Sct star KIC 7106205 (Bowman & Kurtz 2014) where one mode changed in amplitude from 5 to 0.5 mmag in 650 d, then remained stable for the remaining 820 d of the 4-yr data set, while other modes in this star had constant amplitude over the full 1470 d. Yang et al. (2022) studied KIC 2857323, a high-amplitude δ Sct (HADS) star pulsating in the fundamental and first-overtone radial modes. Such stars usually show much more stable pulsation amplitudes than other, lower-amplitude δ Sct stars that pulsate in many modes, yet Yang et al. found a slow, secular decay of the first-overtone amplitude over the 4 yr of the Kepler data set. So even 'simple' δ Sct stars with few pulsation modes can show amplitude changes on a time-scale less than years. Similar to this δ Sct star, Carrell et al. (2024) have shown in TESS and AAVSO data, over a time-scale of 100 d, the disappearance, then reappearance of the first-overtone mode in the double-mode RR Lyr star V338 Boo.

Changes in the pulsation spectra are also common for white dwarf stars. Among the most spectacular events observed was the appearance of a new pulsation mode and the vanishing of all others in the prototype pulsating DB white dwarf GD 358 (V777 Her) within a single day followed by a slow disappearance of this mode (Kepler

et al. 2003). On the other hand, most of the pulsation modes in the pulsating DB white dwarf PG 1456+103 disappeared at some point and were observed to grow back on a time-scale of just a few weeks (Handler & WET network of collaborators 2013).

Abt, Guzik & Jackiewicz (2023) found that the well-known A supergiant star Deneb (α Cyg, HR 7924, HD 197345) ceases (or nearly ceases) pulsating at times, then resumes on perhaps a \sim 70-d time-scale. They demonstrated this in both radial velocity data going back a century and with recent *TESS* (*Transiting Exoplanet Survey Satellite*; Ricker et al. 2015) photometric data. Guzik, Kloppenborg & Jackiewicz (2024) extended this discussion with further data from *TESS* and the American Association of Variable Star Observers (AAVSO). Abt, Guzik & Jackiewicz speculated that the cause of the resumption of pulsation may lie in 'the microvariations produced in convective layers below their atmospheres, pulsation-driven shocks and rarefactions, or pulsation–convection interactions.' These are interesting conjectures, but we do not know the causes of these amplitude variations. At the moment, no other star is known to show this pulsation behaviour seen in Deneb.

Polaris (α UMi, HR 424, HD 8890) is another famous star that shows amplitude modulation of its 4-d Cepheid pulsation. Turner et al. (2005) studied pulsation period changes in Polaris over 160 yr from 1844-2004 and found a steady increase for most of the time span, but with a more rapid decrease from 1963-1966. They found an amplitude greater than 0.1 mag in V up to the 1963–1966 hiatus, followed by a sharp decline to below 0.05 mag with erratic behaviour from cycle-to-cycle. Bruntt et al. (2008) documented a drop in pulsation amplitude in Polaris from 120 to 30 mmag over a century up to the early 2000 s. Dinshaw et al. (1989) detected a steady period increase in 1987–1988 from radial velocity variations. From these studies it appeared that Polaris might have been evolving redward out of the instability strip and stopping pulsation. But Bruntt et al. showed a recovery in amplitude from 2003 to 2006. We have examined the Sector 60 TESS data from 2022 December-2023 January that show clear pulsation with a period 3.973 d and a peak-to-peak amplitude of 76 mmag with the TESS red bandpass. So Polaris is not stopping pulsating at present.

Another famous bright star that showed significant decrease in pulsation amplitude, and was thought to be stopping pulsating, is Spica (Lomb 1978), a spectroscopic binary with a β Cep primary that has been observed to pulsate in several modes, with a primary frequency of $5.75\,\mathrm{d}^{-1}$ (Tkachenko et al. 2016). Subsequent observations – including space-based observations from the MOST (Microvariability and Oscillations of Stars) satellite (Desmet et al. 2009) – have shown that the $5.75\mathrm{-d}^{-1}$ frequency has continued, although at decreased amplitude that has at times been difficult to detect with ground-based observations (see Chapellier et al. 1985).

We have discovered a star that has been observed since the 1980s to have a rich pulsation spectrum, and it has now stopped pulsating completely. To our knowledge, this is the first pulsating star to have been observed to completely cease pulsating. This star is HD 60435, a rapidly oscillating Ap (roAp) star that is the principal subject of this paper.

1.1 Frequency and amplitude variations in roAp stars

The rapidly oscillating Ap (roAp) stars are A to early-F spectroscopically peculiar stars with strong magnetic fields. They typically show stable long-lived rotational light variations caused by spots associated with roughly dipolar magnetic fields that are inclined to the rotation axis. They pulsate in high radial overtone p modes with the pulsation axis inclined to the rotation axis and close to the magnetic axis (e.g.

Bigot & Kurtz 2011). Detailed introductions to these stars can be found in ensemble studies of them in the *TESS* data sets by Cunha et al. (2019) and Holdsworth et al. (2021, 2024), and in a review by Kurtz (2022, section 2.15.12).

Some roAp stars have pulsation modes that have stable frequencies and amplitudes over decades, while others show measurable changes in these quantities on times-scales as short as one day (see Holdsworth et al. 2021, 2024 for examples). An interesting and illustrative case is that of HD 217522. This star was discovered to have pulsations with frequencies near to $105\,\mathrm{d^{-1}}$ (1.22 mHz) in 1981. Later observations in 1989 showed those frequencies plus a new one near $174\,\mathrm{d^{-1}}$ (2.01 mHz) that was not present in 1981. The modes of these frequencies are separated by many radial overtones, with the intervening modes not excited. This excitation of nonconsecutive radial overtone modes remains a more general problem in understanding mode selection in these stars.

Medupe et al. (2015) studied the pulsations in HD 217522 spectroscopically, examining pulsation amplitude line-by-line and as a function of depth in individual lines. Because elements are radially stratified in roAp star atmospheres, this allows the examination of pulsation amplitude as a function of atmospheric depth. The complex modes are magneto-acoustic, as has been examined theoretically in detail by Quitral-Manosalva, Cunha & Kochukhov (2018). Medupe et al. found that the higher frequency seen in the 1989 photometric data of HD 217522 was present at some depths in the atmosphere, but not seen in others. They also pointed out, as have other authors, that this star shows amplitude variability on a time-scale as short as a day.

Thus, we understand that some pulsation modes may be visible at particular atmospheric depths and others not; Quitral-Manosalva et al. (2018) provide theoretical understanding of this. It is important when studying the problem of mode excitation and damping, and in looking for counterparts of stars like Deneb, Spica, Polaris, the δ Sct and roAp stars, and others, that we consider whether different data sets are probing different parts of the stellar atmosphere therefore giving different results, although that is far less likely for low radial overtone pulsators like Deneb, Spica, and Polaris, than for high radial overtone pulsators like the roAp stars.

2 HD 60435, AN ROAP STAR THAT HAS STOPPED PULSATING

HD 60435 is a magnetic Ap star that was discovered to be an roAp star by Kurtz (1984) from observations obtained during 1983 February to April. It was studied extensively by Matthews, Kurtz & Wehlau (1987) using ground-based photometric data in Johnson B obtained contemporaneously from observatories in Chile and South Africa from 1984 November through 1985 March. They found a series of p modes of consecutive radial overtone and alternating even and odd degrees ($\ell=1,2$) for radial overtones ranging from n=13-28, making the star a prime asteroseismic target.

From a study of the rotational light variation caused by stable spots, Kurtz, van Wyk & Marang (1990) determined the rotation period to be $P_{\rm rot} = 7.6793 \pm 0.0006\,{\rm d}^{-1}$ and showed that spots on opposite hemispheres of the star are seen, presumably at, or near to, both magnetic poles. They confirmed the result of Matthews et al. that the pulsation amplitudes vary with the rotation of the star—as expected for an oblique pulsator — but also non-periodically on time-scales shorter than the rotation period.

Zverko, Ziznovsky & North (1998) carried out a spectroscopic study and found variability in the equivalent width of lines of Li, Ca, Fe, and Pr with the rotation period. Their abundance analysis found

typical Ap abundance anomalies with overabundances in some rare earth elements of up to 300 times solar.

Balona, Holdsworth & Cunha (2019) and Holdsworth et al. (2021) both reported studies of *TESS* data for HD 60435 that show pulsation amplitude variations on a time-scale as short as a day. Balona, Holdsworth & Cunha presented a set of plots (their fig. 9) showing amplitude spectra for the data on a 1-d time-scale. While their plots did not account for the 7.68-d rotational variations, the amplitude variations are so strong that the case was clear for rapid changes in mode amplitude.

HD 60435 was observed extensively by the *TESS* mission over a time-span of 5 yr. The star showed significant, albeit variable, pulsation amplitude in a series of even and odd degree modes for the first two years of *TESS* observations, then no pulsation at all, except for a brief resurgence of a single mode during one rotation cycle. Uniquely, at present, this star has stopped pulsating.

2.1 The TESS data

HD 60435 was observed in the years 2018–2023 by *TESS* in some sectors (hereafter abbreviated 'S') from S3–69, while other sectors were not observed. Pre-search Data Conditioning Simple Aperture Photometry (PDCSAP) data are available at 120-s cadence for S3, 6, 7–10, 13, 27, 30, 33–35, 37, 68–69, which cover a time span from 2018 September 20 to 2023 September 20–5 yr. An additional four sectors of full frame image (FFI) 200-s data are available for S61, 62, 63, and 67.

Because we are examining rapid changes in pulsation amplitude, and the total cessation of pulsation, and because we are concerned with the time-scales for these, it is important to show a record of when the star was observed. We also must distinguish between secular pulsation amplitude changes, and those caused by oblique pulsation where the observed amplitude varies with rotation and viewing aspect.

The *TESS* elliptical orbit of Earth is ~ 13.5 d with data downloads at each perigee passage. The sectors comprise two orbits, hence there are usually continuous data strings of one orbit, or half a sector, minus time for the data downloads. There are also changes in the satellite physical conditions with each re-acquisition of the observed field. These lead to some data being removed by the PDCSAP pipeline at the beginnings and ends of each orbit. Fortuitously for the study of HD 60435, the observing strategy gives continuous data sets of up to 14 d, which is close to 2 rotation cycles. This is sufficient to resolve the frequency multiplets (split by the rotation frequency) generated by oblique pulsation.

For our analysis, we therefore divided the data into what we call 'half-sectors'. These are tabulated in an example Table 1 (with the full Table A1 in the Appendix) where they are labelled with the half-sector names (e.g. S3.1, S3.2) and with a time-stamped name giving the truncated BJD (BJD – 2400000.0) of the central time of each half-sector (e.g. JD58390.03 and JD58401.42 for S3.1 and S3.2, respectively). These time-stamped names are used in plots of amplitude spectra in this paper so that the gaps between those can be judged.

Fig. 1 shows a light curve of all of the *TESS* data. The data in the light curve include the rotation and pulsation variations, along with some low-frequency instrumental artefacts, all of which are so compacted at the scale of the figure that they cannot be seen. The purpose of this light curve is to show the time distribution of the data in accompaniment with Tables 1 and A1.

Loumos & Deeming (1978) showed that a time base of $T = 1.5/\Delta f$ is necessary to fully resolve two frequencies separated

Table 1. Times and durations of the *TESS* half-sectors and full sectors. The data files are named with the mid-time of each half-sector for additional identification of the individual amplitude spectra in Figs 4 and A1. Columns 5 and 6 give, respectively, the duration of the half-sectors and their combined sector in days. This table is a sample; the full table is Table A1 the Appendix.

TESS Sector	Data set name	BJD time start	BJD time end	Duratio	on days
		2400	000+	half sector	full sector
3.1	JD58390.03	58 385.934 815	58 394.154 367	8.22	
3.2	JD58401.42	58 396.639 116	58 406.212 895	9.57	20.28
6.1	JD58472.65	58 468.272 565	58 477.021 355	8.75	
6.2	JD58484.18	58 478.243 596	58 490.045 204	11.80	21.77
7.1	JD58497.34	58 491.634 114	58 503.038 448	11.40	
7.2	JD58510.40	58 504.710 685	58 516.087 190	11.38	24.45

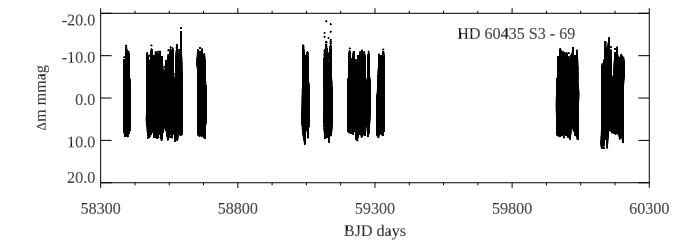


Figure 1. A light curve of the S3–69 *TESS* PDCSAP data. This includes the rotational variations as well as the pulsation, although neither can be discerned at the resolution of the 5-yr span of the data. This plot accompanies Table A1 to show the time span and gaps in the observations. The time shown is BJD – 2400000.

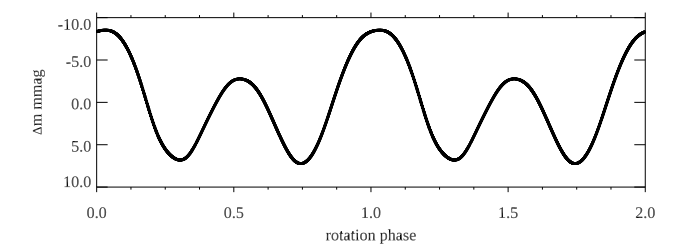


Figure 2. The rotation curve. Two cycles are shown. $P_{\text{rot}} = 7.679696 \pm 0.000005 \,\text{d}$. The rotational curve was generated from a 10-harmonic fit of the rotation frequency to the entire data set, but then sampled at the same times as the S7 observations for illustrative purposes.

by Δf in a given data set, and to determine their amplitudes and phases without systematic error. It can be seen in Table A1 that most of the half-sectors have sufficient duration to resolve the rotational modulation of the pulsation amplitudes by this criterion.

3 THE ROTATION AND MAGNETIC FIELD

Fig. 2 shows the light variability caused by the stable spots, as is typical of α^2 CVn stars. These stars are known to have stable rotational variations from the spots and stable magnetic fields for observations spanning nearly a century for some stars. Importantly for HD 60435, that rotational variability is completely stable over the time-span of the data, implying that there is no change in the spots or magnetic field that might impact on the pulsations. The spot variations in the S3–69 data yield an improved rotation period of $P_{\rm rot}=7.679696\pm0.000005\,{\rm d}$, both more precise and also in agreement with previous determinations.

It is worth noting that roAp stars observed in Johnson *B* usually show pulsation maximum near to rotational light minimum; i.e. the

spots that cause the rotational light variations lie close to the poles of the pulsation axis. Often for Ap stars the rotational variation is a maximum in the red when it is minimum in blue. That is caused by flux redistribution in the spots as a consequence of the increased temperature gradient caused by the line opacity of the rare earth elements. This relationship between the maxima in red and minima in blue light for HD 60435 is shown clearly to be the case in fig. 2 of Kurtz et al. (1990), who studied the rotational light variations of this star through *UBVRI* filters.

We assume here that the axes of the magnetic field and pulsation coincide, or nearly coincide (Bigot & Kurtz 2011), and that the spots are close to the magnetic poles. We also assume that the epoch of pulsation maximum, BJD 2458500.53070, as derived from the oblique pulsator model in Section 6 below, also nearly coincides with the time of rotational light maximum, caused by the spots. These assumptions are justified in the results to come below. We then find an ephemeris for the times of pulsation, magnetic field, and rotational light maxima to be:

$$t_{\text{max}} = \text{BJD} \, 2458500.53070 + 7.679696 \pm 0.000005 \times E \,.$$
 (1)

Hubrig et al. (2006) measured a longitudinal magnetic field of $B_\ell = -296 \pm 52\,\mathrm{G}$ at BJD = 2453000.072. Using equation 1 we find that the fractional rotational phase of the Hubrig et al. longitudinal magnetic field measurement is $\Phi = 0.234 \pm 0.005$, which is essentially in quadrature. In the standard oblique rotator model (e.g. Stibbs 1950; Preston 1967), for a dipole field the longitudinal field measured varies as

$$B_{\ell} = \frac{1}{20} \frac{15 + u}{3 - u} B_{\rm p}(\cos \beta \cos i + \sin \beta \sin i \cos(2\pi \Phi)), \qquad (2)$$

where u is a limb-darkening coefficient. In sections 6 and 7 below, we derive the rotational inclination to be $i=53^\circ$ and the magnetic obliquity to be $\beta=63^\circ$ from the oblique pulsator model. Assuming the magnetic and pulsation axes to be closely aligned, and taking u=0.5 yields a polar field strength of $B_{\rm p}\approx 2.8\,{\rm kG}$, which is acceptably close to the asteroseismic polar field strength of $B_{\rm p}\approx 4\,{\rm kG}$ we derive in Section 8 below from modelling the quadrupole pulsation amplitude and phase variations with rotation.

Further measurements of the longitudinal magnetic field strength in HD 60435 are desirable.

4 AMPLITUDE SPECTRA

To study the pulsation frequencies, amplitudes, and changes in those amplitudes we generated amplitude spectra using the rapid Fourier transform algorithm of Kurtz (1985). The pulsation frequencies are well separated from the low-frequency rotation variations and instrumental artefacts, so we ran a high-pass filter to remove all the low frequency variation – both astrophysical and instrumental – so

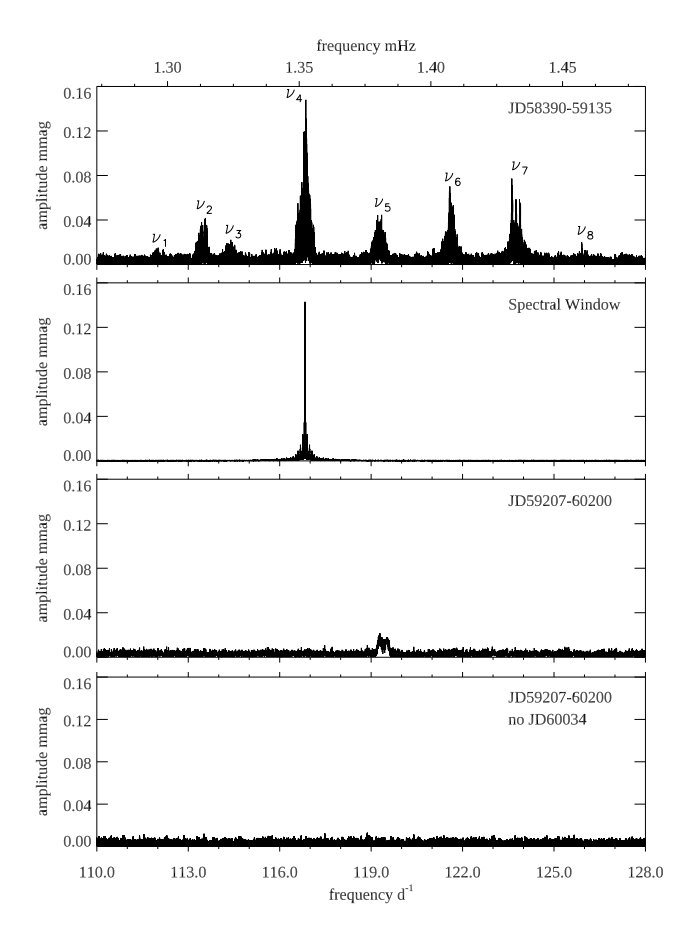


Figure 3. Top: Amplitude spectrum over a time-span of 755.5 d when the star was showing pulsations. The mode frequency peaks, which are broadened by amplitude modulation, are labelled as ν_1 to ν_8 for discussion. Second panel: The spectral window for ν_4 . Third panel: Amplitude spectrum over a time span of 1004 d after the pulsations ceased, except for a brief reappearance of ν_5 in the half-sector JD60034.25 (see Fig. A1). Bottom: The same as the third panel, but with the half sector JD60034.25 left out. Even with the non-periodic amplitude modulation the rotational triplet structure of ν_7 is evident in the top panel.

that the noise in the amplitude spectrum is white. This allows better determination of the uncertainties on frequency, amplitude, and phase by least-squares fitting, and it removes the high-frequency tail of the spectral window pattern of the low-frequency peaks, which have much higher amplitude than the pulsations. The high-pass filter was a simple sequential pre-whitening of low-frequency peaks up to $4\,\mathrm{d}^{-1}$ until the noise level at higher frequencies was reached. Throughout the rest of this paper the data analysed for the pulsation frequencies are those high-pass filtered data.

To set the stage, the top panel of Fig. 3 shows an amplitude spectrum for the combined S3–30 data where strong, amplitude-variable pulsation is seen in many modes. Because of the rotational modulation caused by oblique pulsation, and the amplitude modulation on a short time-scale, the peaks are broadened; they are labelled as ν_1 to ν_8 in the top panel for discussion. To show the broadening, the spectral window for ν_4 is shown in the second panel. The third panel shows the amplitude spectrum of the S33–69 data where there is no pulsational signal, except for ν_5 , which only appeared at the end of data set JD60034.25 (S63.2). When that half sector is left out the bottom panel shows a complete absence of pulsation over a time span of 1004 d.

Because of the broadened peaks caused by amplitude modulation as shown in Fig. 3, the frequencies were estimated from the broadened peaks in the amplitude spectra of the half-sectors of data when they were excited to observable amplitude. ν_1 , ν_3 , ν_4 , and ν_5 were measured from the JD58390.03 data; ν_2 was measured from JD58675.49 data; ν_6 and ν_7 were taken from the central frequencies of the rotational multiplets given in Table 6 from the combined half-sectors JD58497.34 and JD58510.40; ν_8 was measured from the JD58549.94 data.

Table 2 shows a comparison between the ground-based frequencies found by Matthews et al. (1987) and the *TESS* frequencies found in this study. The uncertainties given are the formal errors determined from the data subsets (chosen as explained above) because of the amplitude modulation broadening of the peaks in the amplitude spectra, as seen in Figs 4 and A1. These uncertainties appear reasonable, given the good agreement between the *TESS* and ground-based values for six of the frequencies in data taken decades apart in time.

Other than those 6 frequencies, most of the rest of the ground-based frequencies are outside of the frequency range of detected peaks in the *TESS* data. Taylor et al. (1993) obtained 5.5 h of high-speed photometric observations of HD 60435 in the ultraviolet with the Hubble Space Telescope. They found one certain pulsation mode frequency at $123.70\,\mathrm{d}^{-1}$, which corresponds to the ν_7 dipole frequency seen in Fig. 3, showing that HD 60435 was pulsating in 1991 August. The other possible mode frequencies they suggested do not have counterparts in Table 2.

For the TESS data, Table 2 also shows that there is a series of alternating even-and-odd degree modes with separation of \sim 28 µHz, hence the large separation is 56 µHz. Many of the ground-based frequencies that have no counterpart in the TESS data show separations around 52 µHz, suggesting that those may be from consecutive modes of the same degree. Because of the challenges caused by the complex spectral windows for the ground-based data, we do not use those further in this analysis. We return to identifying the degrees of the modes for the TESS data from models in Section 7 below.

Fig. 4 shows a sample of the amplitude spectra for each of the half-sector data strings given in Table 1 (the full set of amplitude spectra are in Fig. A1 of the Appendix), where extreme changes in pulsation amplitude for various modes can be seen. It is notable that when the ν_4 pulsation is present, the ν_6 and ν_7 pulsations are not, and vice versa. This gives the appearance of mode switching via energy transfer between these modes, but the complete disappearance of all pulsation in the S33–69 data shows the situation is more complex. Clearly, the pulsation energy in the observed modes is not conserved.

4.1 Tracing the amplitude changes during the *TESS* observations

The amplitude changes in HD 60435 and the cessation of pulsation are the most important results of this paper. It is useful to have complementary ways of viewing these changes, as we try to understand their causes and consequences; thus, we present the amplitude changes in three separate ways. The first method is the traditional amplitude spectrum views in Figs 4 and A1 presented in the last section. The other two methods we present in this section are least-squares fits of the five most prominent pulsation frequencies to short sections of the data, and a wavelet analysis.

4.1.1 Amplitude changes seen with least-squares fits

To describe the changes in amplitude of the five strongest pulsation modes of HD 60 435 in more detail, we subdivided the *TESS* data into

2108 D. W. Kurtz et al.

Table 2. Comparison between the ground-based *B*-data frequencies of Matthews et al. (1987) and the *TESS* frequencies measured for ν_1 to ν_8 . The sixth column shows the frequency differences, which are used to determine the large frequency separation, $\Delta\nu_0=56\,\mu\text{Hz}$. The final column shows the observed ratios discussed in Section 7.

Label	Ground-bas	sed frequency	TESS	frequency	Frequency difference	$r_{ m obs}$
mI	mHz	d^{-1}	d^{-1}	mHz	μHz	μHz
	0.7090	61.2576				
	0.7614	65.7850				
	0.8428	72.8179				
	0.9397	81.1901				
	0.9906	85.5878				
	1.0433	90.1411				
	1.0990	94.9536				
	1.1482	99.2045				
	1.1734	101.3818				
	1.2250	105.8400				
	1.2848	111.0067				
ν_1			112.16 ± 0.14	1.29814 ± 0.00162	$v_2 - v_1 = 14.2$	
ν_2			113.39 ± 0.04	1.31235 ± 0.00046	$v_3 - v_2 = 12.1$	
ν_3	1.3281	114.7478	114.43 ± 0.05	1.32447 ± 0.00058	$v_3 - v_1 = 26.3$	-0.01 ± 0.02
ν_4	1.3525	116.8560	116.83 ± 0.02	1.35221 ± 0.00023	$v_4 - v_3 = 27.7$	
ν_5	1.3810	119.3184	119.35 ± 0.04	1.38137 ± 0.00046	$v_5 - v_4 = 29.2$	0.02 ± 0.01
ν_6	1.4073	121.5907	121.62 ± 0.01	1.40760 ± 0.00012	$v_6 - v_5 = 26.2$	
ν_7	1.4334	123.8458	123.77 ± 0.01	1.43248 ± 0.00012	$v_7 - v_6 = 24.9$	0.00 ± 0.01
ν_8	1.4572	125.9021	125.91 ± 0.09	1.45728 ± 0.00104	$v_8 - v_7 = 24.8$	

small subsets. To assure that the frequencies are resolved, we took the frequency separation to be 28 μ Hz which requires data time spans of 0.6 d to fulfil the Loumos & Deeming (1978) criterion, $T=1.5/\Delta f$. Conservatively, we chose data time spans of 0.7 d. The run of the pulsation amplitudes of five modes is shown in Fig. 5. They are ν_2 , ν_4 , ν_5 , ν_6 , and ν_7 as listed in Table 2. The amplitudes of ν_1 , ν_3 , and ν_8 are too small to be traced meaningfully in this way. The short time-scale amplitude modulations of the modes are evident, as is especially the cessation of pulsation for all modes from BJD 2459200, with the exception of a brief return of ν_5 around BJD 2460037. Fig. 5 demonstrates that amplitude variations of individual modes occur on time-scales shorter than a single rotation period.

4.1.2 Amplitude changes with a wavelet analysis

The third method of viewing the amplitude changes with time is with a wavelet analysis. Using the Astropy¹ implementation of the Lomb–Scargle periodogram (Astropy Collaboration et al. 2022) we calculated a sliding window amplitude spectrum to illustrate the mode evolution over time. To do this, we convolved the time series with a sliding rectangular window of width 0.8 d, at steps of 0.5 d. By testing, we found that smaller window sizes result in moderately decreased frequency resolution, whereas larger sizes show the changes in the modes less well. We also experimented with using a Gaussian window, but found only minor differences with the rectangular window approach. In each segment of the light curve, we calculated the amplitude spectrum between 105 and 135 d⁻¹ with an oversampling factor of 5. We performed the analysis for each sector individually and show the results in Figs 6 and A2.

4.1.3 The harmonic and the 20-s data

There is a second harmonic observable when ν_4 is near its greatest amplitude. That is visible in the 120-s data. There are 20-s cadence

¹http://www.astropy.org

data available in S27, 30, 33–35, 37, but given the amplitude modulation, we make no astrophysical inference from this second harmonic, except to mention that it is observed to be present, which is common for many roAp stars; see Holdsworth et al. (2021, 2024) for examples.

4.2 Further ground-based observations

To test whether pulsations had restarted, we used the Las Cumbres Observatory Global Telescope (LCOGT) network of telescopes (Brown et al. 2013) to observe HD 60435 through a Johnson *B* filter for 0.5–1.0 h over 10 nights in 2023 December and 2024 January. All observations were collected with one of the 0.4-m telescopes at Siding Spring Observatory, Australia, using the QHY camera in full frame mode. The data were reduced and aperture photometry performed with an adapted version of the TEA-Phot reduction code (Bowman & Holdsworth 2019).

A journal of the observations is given in Table 3. The LCOGT observations span 98–110 d after the last of the *TESS* observations, and they cover near two rotations of HD 60435. From equation (1), we calculate the rotation phase of the mid-point of each nightly run, as seen in column 3 of Table 3. Several nights were near to rotation phase zero, which is rotational light maximum, hence pulsation maximum. In the past, HD 60435 has had peaks in the amplitude spectrum as great as 6 mmag in Johnson *B* observations (Kurtz 1984), although Matthews et al. (1987) generally found peaks near 3 mmag during pulsation maximum. As can be seen from Table 3 the noise peaks range between 2.1–3.5 mmag on the nights where observations were near rotation and pulsation maximum, suggesting that HD 60435 had not returned to pulsating during the time span of our new *B* observations.

4.3 Pulsational radial velocity variations

HD 60435 was observed with the High Resolution Spectrograph (HRS; Bramall et al. 2010; Crause et al. 2014) on the Southern African Large Telescope (SALT; Buckley, Swart & Meiring

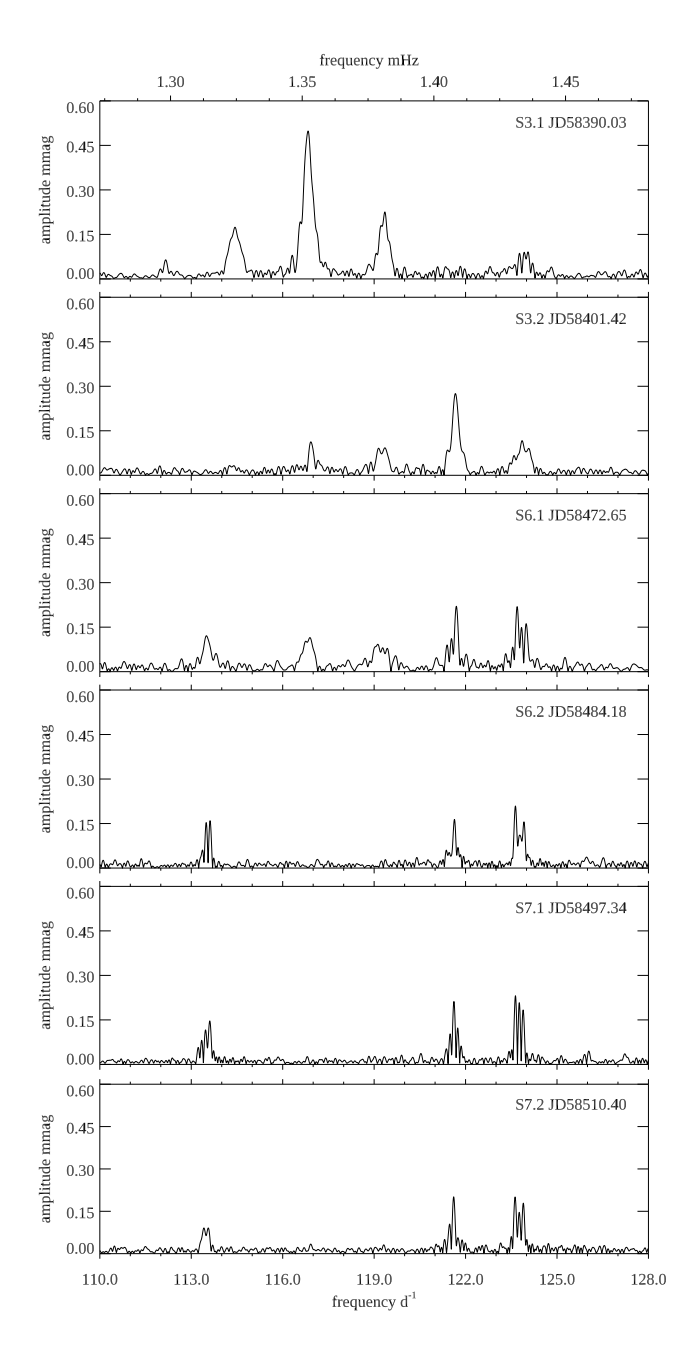


Figure 4. Example amplitude spectra of the half-sectors showing the amplitude modulation and mode changes. The full set of amplitude spectra for all of the half-sectors is shown in Fig. A1 in the Appendix.

2006) on four separate nights in 2014 – 2015. HRS is a dual-beam spectrograph with wavelength coverage of 3700–5500 Å and 5500–8900 Å. The observations were automatically reduced using the SALT custom pipeline, which is based on ESO's MIDAS pipeline (Kniazev, Gvaramadze & Berdnikov 2016, 2017). Observations were made under the proposal code 2014-2-SCI-068 (PI: Medupe), and were collected in the Medium Resolution mode ($R \sim 45\,000$) with exposure times of 70 s resulting in a cadence of 113 s. Table 4 gives a journal of the observations.

For the pulsation analysis, we normalized the spectra using the SUPPNET code (Różański et al. 2022) and treated each night separately. Ions of the rare earth elements are typically stratified in the atmospheres of roAp stars, and there is often detectable pulsation amplitude seen in lines of Nd III (see, e.g. Ryabchikova et al. 2007; Elkin, Kurtz & Mathys 2005). We identified lines of Nd III that were locally isolated and had sufficient equivalent width for cross-correlation. This resulted in the use of seven lines at $\lambda\lambda$: 5802.53, 5845.02, 5851.54, 5987.68, 6145.07, 6327.26, and 6550.23 Å. The central wavelength and equivalent width (0th moment) of each line was measured by the moment method (Aerts, de Pauw & Waelkens 1992). These were constructed into a δ -function template using the wavelengths as positions and the equivalent widths as the depth to weight the lines (see Wright 2008). Cross-correlation with this template produced line profiles that combine the information of the variation from all the lines chosen. From the cross-correlation profiles the radial velocity measurements were made using the first moment (Aerts et al. 1992).

Fourier analysis of the resultant radial velocities showed a clear detection of pulsation on night 4 with a semi-amplitude of $385 \pm 35 \,\mathrm{m\,s^{-1}}$, when the rotation phase of 0.04 is at the expected time of pulsation amplitude maximum. There are tentative detections on two of the other nights (Fig. 7). While the frequency resolution and limited number of observations do not allow for a detailed study, they do allow us to confirm that the star was pulsating during the observation period in 2014–2015, 30 yr after the seminal observations of Matthews et al. (1987), and 4 yr prior to the beginning of the *TESS* data analysed in this paper.

5 FUNDAMENTAL DATA

From Gaia DR3 (Gaia Collaboration 2016a, 2023a; Creevey et al. 2023), we find $T_{\text{eff}} = 7800 \,\text{K}$, $\log g = 4.06 \,(\text{cgs})$, [Fe/H] = -0.08. Using the Infrared Flux Method (IRFM), Smalley (private communication) found $T_{\rm eff} = 7900 \pm 200$ K. The TESS Input catalogue (TIC) gives $T_{\text{eff}} = 8150 \,\text{K}$, $\log g = 4.13$. There are two published spectral types for HD 60435. One is ApSr(Eu) from the Michigan Spectral Catalog (Houk & Cowley 1975), which does not give a spectral subtype from which $T_{\rm eff}$ could be inferred. This is not unusual for Ap stars, as their abnormal line strengths confound giving a temperaturerelated subclass. The other spectral classification is A3 from the original Henry Draper (HD) Catalog from over a century ago with an updated reference of Cannon & Pickering (1993). That would imply $T_{\rm eff} \sim 8700 \, {\rm K}$, but we give that low weight as a consequence of the low resolution of the HD catalog. The other values for $T_{\rm eff}$ are consistent within the uncertainties. We adopt $T_{\rm eff} = 7900 \pm 200 \, {\rm K}$ based on the result from the IRFM. The Gaia and TIC surface gravities are consistent.

To infer the luminosity, equatorial rotational velocity, and the inclination of the rotation axis, we ran a Monte Carlo simulation with 10^6 draws. The uncertainties on each parameter were calculated as percentiles 15.86 and 84.14 of the Monte Carlo simulations. From *Gaia* DR3, we adopted the parallax and its uncertainty, $\pi = 4.077 \pm 0.014$ mas, mean apparent g magnitude $g = 8.87 \pm 0.01$ mag with an assumed uncertainty. The interstellar extinction in the *Gaia* g band may be as large as $A_g = 0.14$ as derived by the *Gaia* DR3 pipeline for hot stars (Fouesneau et al. 2023). With that extinction the absolute G magnitude was calculated as

$$G = g - 5 \left[\log_{10} \left(\frac{1000}{\pi} \right) - 1 \right] - a_g.$$
 (3)

We used a bolometric correction of zero (which is appropriate for $T_{\rm eff} = 7900 \, {\rm K}$) and calculated the luminosity,

$$L/L_{\odot} = 10^{-(G-M_{\text{bol},\odot})/2.5}$$
, (4)

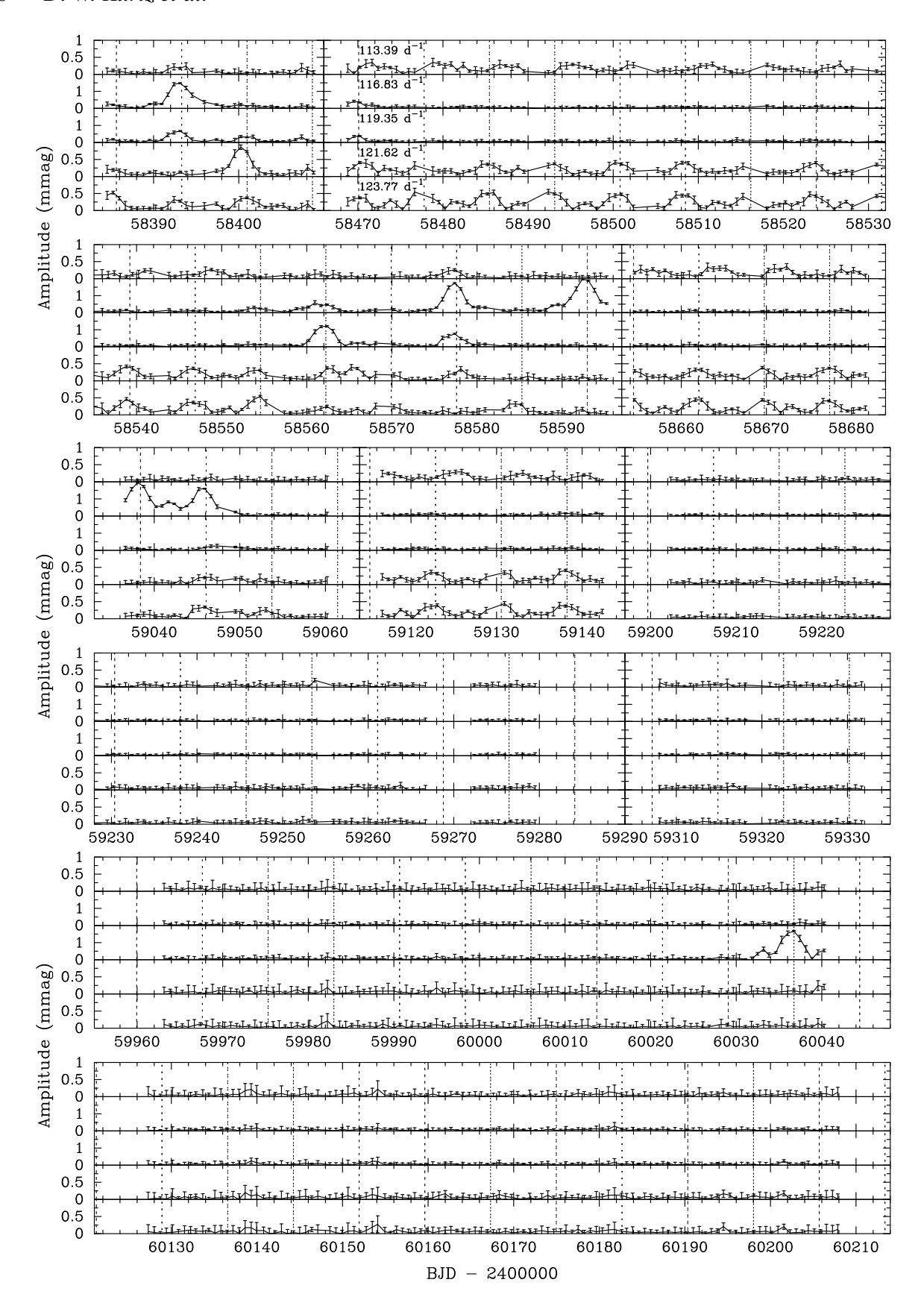


Figure 5. The run of the amplitudes of the five strongest pulsation modes $-\nu_2$, ν_4 , ν_5 , ν_6 , and ν_7 – of HD 60 435 over time. The error bars are formal values computed according to Montgomery & O'Donoghue (1999). Vertical dashed lines denote times of rotational light maximum in the *TESS* bandpass.

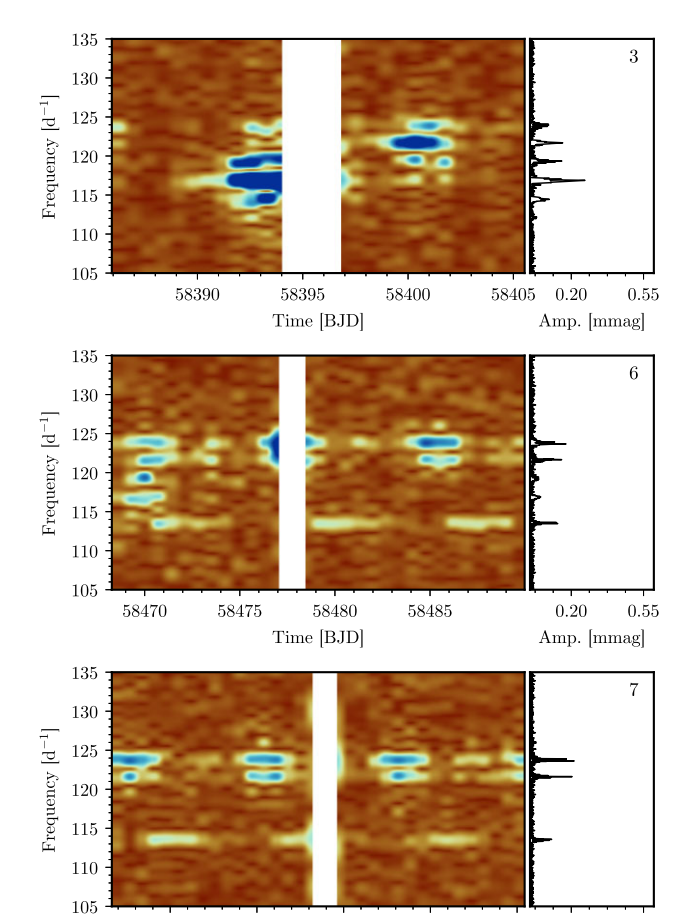


Figure 6. Example wavelet plots by sector. The time is BJD -2400000. The amplitude modulations from both the changing view of oblique pulsation with the 7.679696-d rotation and the secular changes can be seen. The colours range linearly from amplitude zero (red) to amplitude 0.6 mmag (blue). The sectors are numbered in the top right corner of each plot. The full set of plots are in Fig. A2 in the Appendix.

Time [BJD]

58510

58515 0.20

Amp. [mmag]

58495

Table 3. A journal of the LCOGT Johnson *B* observations. The BJD is the mid-point of the nightly run. The third column is the rotation phase at that BJD; the fourth column is the duration of the observing run. The integration time was 10.5 s. The final column gives the height of the highest noise peaks in the amplitude spectrum of the observations each night in the frequency range of the previously known pulsation of HD 60435.

Date	BJD -2400000.0	Rot. phase	Δt h	N	A _{max} mmag
2023 - 12 - 25	60 303.990 55	0.83	0.68	89	3.5
2023 - 12 - 25	60 304.200 83	0.86	0.49	138	2.7
2023 - 12 - 26	60 305.159 51	0.99	0.99	127	2.5
2023 - 12 - 27	60 306.022 35	0.10	0.49	130	1.8
2023 - 12 - 28	60 307.147 24	0.25	0.98	124	11.3
2023 - 12 - 30	60 309.022 37	0.49	0.98	126	2.4
2024 - 01 - 01	60 311.102 57	0.76	0.98	138	1.7
2024 - 01 - 02	60 312.040 46	0.88	0.98	134	2.1
2024 - 01 - 03	60 313.035 87	0.01	0.98	133	2.8
2024 - 01 - 05	60 315.021 72	0.27	0.95	128	1.4
2024 - 01 - 06	60 316.017 48	0.40	0.74	94	8.1

Table 4. A journal of the SALT HRS observations. The BJD is the mid-point of the nightly run. The third column is the rotation phase at that BJD; the fourth column, N, is the number of exposures. The integration time was $70 \, \text{s}$ and the cadence was $113 \, \text{s}$.

Date	BJD -2400000.0	Rot. phase	N	Duration s
2014 - 11 - 08	56 969.501 843	0.64	23	2556
2014 - 11 - 09	56 970.506 103	0.77	23	2556
2014 - 12 - 23	57 014.611 339	0.51	24	2669
2015 - 01 - 03	57026.345736	0.04	23	2556

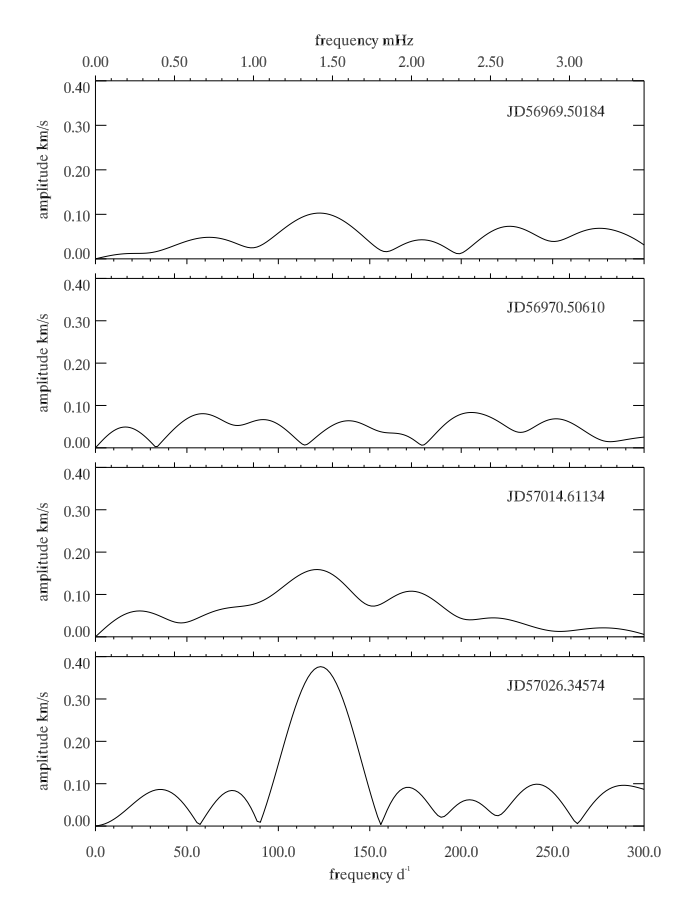


Figure 7. Amplitude spectra of the pulsational radial velocity results from the four nights of SALT observations. It is clear that on the fourth (bottom panel) night that the star is pulsating within the expected frequency range.

where $\rm M_{bol,\odot}=4.74$ is the bolometric luminosity of the Sun. We thereby arrived at a stellar luminosity of $L=15.25\pm0.21\,\rm L_\odot$. Taking the solar $T_{\rm eff}=5772\,\rm K$, we used our luminosity and adopted $T_{\rm eff}$ to calculate a radius, $R=2.08\pm0.10\,\rm R_\odot$. With our measured rotation period of $P_{\rm rot}=7.679696\pm0.000005\,\rm d$, this allowed us to calculate the equatorial rotation velocity, assuming zero flattening, via

$$v_{\rm eq} = \frac{2\pi R}{P_{\rm rot}} \tag{5}$$

to be $v_{\rm eq}=13.8\pm0.7\,{\rm km\,s^{-1}}$. We will use this to calculate the stellar inclination angle in Section 6.

2112 D. W. Kurtz et al.

Table 5. Log of observations from Veloce at AAT. Uncertainties are 1σ level values drawn from MCMC samples.

Date	JD -2400000.0	Radial velocity km s ⁻¹	$v \sin i$ $km s^{-1}$
2023 - 12 - 25	60 304.115 52	19.22 ± 0.09	10.97 ± 0.30
2023 - 12 - 25	60 304.130 29	19.22 ± 0.09	10.96 ± 0.29
2023 - 12 - 26	60 305.143 78	19.22 ± 0.10	10.98 ± 0.29
2023 - 12 - 26	60 305.240 39	19.22 ± 0.11	10.97 ± 0.29
2023 - 12 - 27	60 306.128 76	19.22 ± 0.10	10.97 ± 0.29
2024 - 05 - 23	60 453.857 50	19.22 ± 0.08	10.94 ± 0.30
2024 - 05 - 23	60 453.872 16	19.22 ± 0.09	10.93 ± 0.30
2024 - 05 - 23	60 453.892 24	19.22 ± 0.08	10.95 ± 0.29
2024 - 05 - 23	60 453.906 90	19.22 ± 0.09	10.94 ± 0.29
2024 - 05 - 23	60 453.922 10	19.22 ± 0.09	10.94 ± 0.29
2024 - 05 - 23	60 453.936 76	19.22 ± 0.09	10.95 ± 0.29

5.1 Spectroscopic monitoring

We conducted spectroscopic observations of HD 60 435 using the *Veloce* spectrograph at the Anglo-Australian Telescope, using the *Verde* arm (4420–5960 Å), which is an extension to the established *Veloce Rosso* (Gilbert et al. 2018) instrument. *Veloce* is a high-resolution ($R = 80\,000$) échelle spectrograph using a 19-fibre Integral Field Unit (IFU) that is rearranged into a pseudo-slit. We conducted the observations without simultaneous calibration and performed a simple data extraction that co-adds flux from all object fibres.

HD 60435 was observed five times during three nights in 2023 December (JD 2460304.12-2460306.13) and six times on 2024 May 23 (JD 2460435.86–2460435.94). Table 5 provides a log of these observations. The spectra were normalized on an order-by-order basis using iSpec (Blanco-Cuaresma et al. 2014; Blanco-Cuaresma 2019). After heliocentric correction, we derived stellar line profiles from each échelle order via a least-squares deconvolution (LSD) analysis (Donati & Collier Cameron 1997) using LSDPY package² against a δ-function atomic line mask derived from the Vienna Atomic Line Database (VALD; Kupka, Dubernet & VAMDC Collaboration 2011). A master profile was created for each spectrum by taking an average of LSD profiles weighted by flux uncertainties and omitting regions with strong lines (Na_I D lines, H_{β} , and H_{γ} red wing). Resulting profiles were fitted with a profile created as a convolution of intrinsic profile ($T_{\rm eff}$ and micro-turbulent velocity), instrumental profile, and broadening kernel, yielding a measurement of radial velocity and projected rotational velocity, $v \sin i$. For spectroscopic analysis, we assumed atmospheric parameters $T_{\rm eff}$, log g, and [M/H] from Gaia DR3 (Gaia Collaboration 2016a, 2023a; Creevey et al. 2023).

Individual results of radial velocity and $v\sin i$ are presented in Table 5. There was no radial velocity value in the *Gaia* archive, but our values, measured 0.4-yr apart, are consistent at $19.22\,\mathrm{km\,s^{-1}}$. Combining measurements from 11 independent observations, we measured $v\sin i=11.0\pm0.6\,\mathrm{km\,s^{-1}}$, with the uncertainties conservatively drawn from MCMC samples added in quadrature with a systematic noise floor estimated to be $0.5\,\mathrm{km\,s^{-1}}$ following Houdebine (2011). We use that measured $v\sin i$ to constrain the rotation inclination in Section 6 below. We also find no indication of binarity in our 0.4-yr of radial velocity measurements. This is unsurprising, as the incidence of binarity in Ap stars on a time-scale shorter than that is low (Schöller et al. 2012).

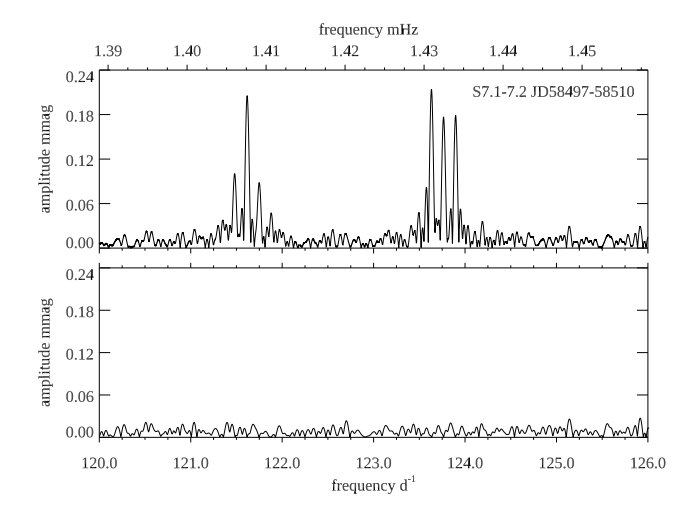


Figure 8. Top: Amplitude spectrum for the S7.1 and S7.2 data over a time-span of $24.45\,d$ showing two multiplets, the one on the left for a quadrupole mode, the one on the right for a dipole mode. Bottom: Amplitude spectrum of the residuals after pre-whitening by a quintuplet and a triplet exactly split by the rotation frequency, as given in Table 6. These frequencies are stable during this time-span. There is no significant signal left. The highest peaks in the residuals are $27\,\mu mag$.

6 APPLICATION OF THE OBLIQUE PULSATOR MODEL TO TWO S7 MULTIPLETS

Some of the half-sectors seen in Figs 4 and A1 show stable pulsation amplitude and rotationally split multiplets from oblique pulsation. The best example of that is for the S7.1 JD58497.34 and S7.2 JD58510.40 data sets where there are two multiplets with no amplitude modulation – other than the oblique pulsator rotational modulation – during the time span of the full sector. Fig. 8 shows an oblique pulsation dipole mode triplet for ν_7 and a distorted quadrupole mode quintuplet for ν_6 .

Table 6 gives the values for the frequencies of these multiplets where the splitting has been chosen to be exactly the rotation frequency. The phases of the dipole v_7 rotational sidelobes were set equal at $t_0 = \text{BJD}\ 2458500.53070$, which is very close to rotational (spot) maximum, hence, by inference, magnetic maximum. This is typical of oblique pulsators. Note that, the phase of the central peak is close to that of the sidelobes, indicating that the mode is nearly a pure dipole. Note also that, the phases of the v_6 quintuplet components are also nearly equal, showing that this mode also has maximum amplitude at rotational light maximum, as does the dipole mode.

Fig. 9 shows the rotational light curve and the pulsation amplitudes and pulsation phases as a function of rotation phase for the dipole triplet and quadrupole quintuplet. As explained in the caption to Fig. 2 above, the rotational curve was generated from a 10-harmonic fit of the rotation frequency to the entire data set, but then sampled at the same times as the S7 observations. Similarly, the pulsation amplitudes and phases were derived from data generated at the times of observations using the frequencies, amplitudes and phases from Table 6. Thus, the noise has been removed from these data for better clarity in the figure.

The rotation curve is slightly non-sinusoidal, which is described by the significant harmonics of the rotation frequency that were input to generate the curve. In particular, the principal maximum at rotation phase zero (or 1 or 2, since the curve is shown through two rotations) is broadened and slightly offset from the pulsation mode maxima. This shows that the abundance spots that cause the rotational

²https://github.com/folsomcp/LSDpy

Table 6. A least squares fit to the S7.1 and S7.2 data of the frequency quintuplet for the distorted quadrupole mode (top five frequencies), and the frequency triplet for the dipole mode (bottom three frequencies) as shown in Fig. 8 where the rotational sidelobes have been forced to be equally split from the central mode frequency by exactly the rotation frequency, $v_{\rm rot} = 0.13021349 \,\mathrm{d}^{-1}$ ($P_{\rm rot} = 7.679696 \,\mathrm{d}$). The zero point for the phases, $t_0 = \text{BJD}\,2458500.53070$, was chosen to be a time when the phases of the two rotational sidelobes of the dipole triplet are equal. Note that, the phase of the central frequency of the dipole, which is the mode frequency, is also equal (within the uncertainty) at this time, showing that the mode is essentially a pure dipole mode. We note that the phases for the quintuplet are all nearly equal at this t_0 , also. This shows that the quadrupole and dipole reach maximum observed amplitude at the same time, and, as we show in Section 4 this is close to the time of maximum rotational light, hence the pulsation poles are close to the spots, therefore most probably the magnetic poles.

d^{-1}	Frequency mHz	Amplitude mmag ±0.007	Phase radians
121.3565	1.4046	0.031	-0.056 ± 0.227
121.4868	1.4061	0.069	-0.467 ± 0.101
121.6170	1.4076	0.193	-0.187 ± 0.036
121.7472	1.4091	0.066	-0.593 ± 0.106
121.8774	1.4106	0.037	-0.340 ± 0.189
123.6345	1.4310	0.199	2.615 ± 0.035
123.7647	1.4325	0.137	2.476 ± 0.051
123.8949	1.4340	0.163	2.615 ± 0.043

variation are spread somewhat away from the pulsation poles, which are themselves most likely very near the magnetic poles. It is not uncommon for spots in magnetic Ap stars (α^2 CVn stars) to have a rough symmetry about the magnetic poles, but to be more complex than that.

The rotational variations show that spots at both magnetic poles are seen, as was deduced by Matthews et al. (1987) in their original study of this star. The dipole amplitude and phase variations are representative of a nearly pure dipole mode. The larger and smaller maxima show that neither the rotational inclination, i, nor the obliquity of the pulsation axis, β , is 90°. If either of those were 90°, we would see equal pulsation maxima at half-rotation intervals. Furthermore, the pulsation amplitude goes nearly to zero at rotation quadrature and the pulsation phase reverses by π rad, as expected for a pure dipole pulsation. We can therefore put a constraint on i and β .

For a dipole oblique pulsation (Kurtz 1982) and using the values in Table 6:

$$\frac{A_{-1}^{(1)} + A_{+1}^{(1)}}{A_0^{(1)}} = \tan i \tan \beta = 2.64 \pm 0.15.$$
 (6)

In Section 5, above we found $v \sin i = 11.0 \pm 0.6 \text{ km s}^{-1}$ observationally and we calculated that $v_{\rm eq} = 13.8 \pm 0.7 \, \text{km s}^{-1}$ from values of R and $P_{\rm rot}$. We thus determine that $\sin i = 0.80 \pm 0.06$ the rotational inclination is $i = 53^{\circ} \pm 6^{\circ}$. With $i = 53^{\circ}$ the constraint of equation 6 then gives $\beta = 63^{\circ} \pm 9^{\circ}$. These values are important inputs to our models in Section 8.

The sum $i + \beta = 116^{\circ} > 90^{\circ}$, showing that we see both pulsation poles over the rotational cycle. This is consistent with the double-wave rotational light curve seen in the top panel of Fig. 9. The pulsation maxima for the dipole mode occur when the pulsation pole comes closest to the line of sight. For the most favourable view at rotation phase zero the pulsation pole is $|i - \beta| = \alpha = 10^{\circ}$ from the line of sight. The secondary pulsation maximum occurs when

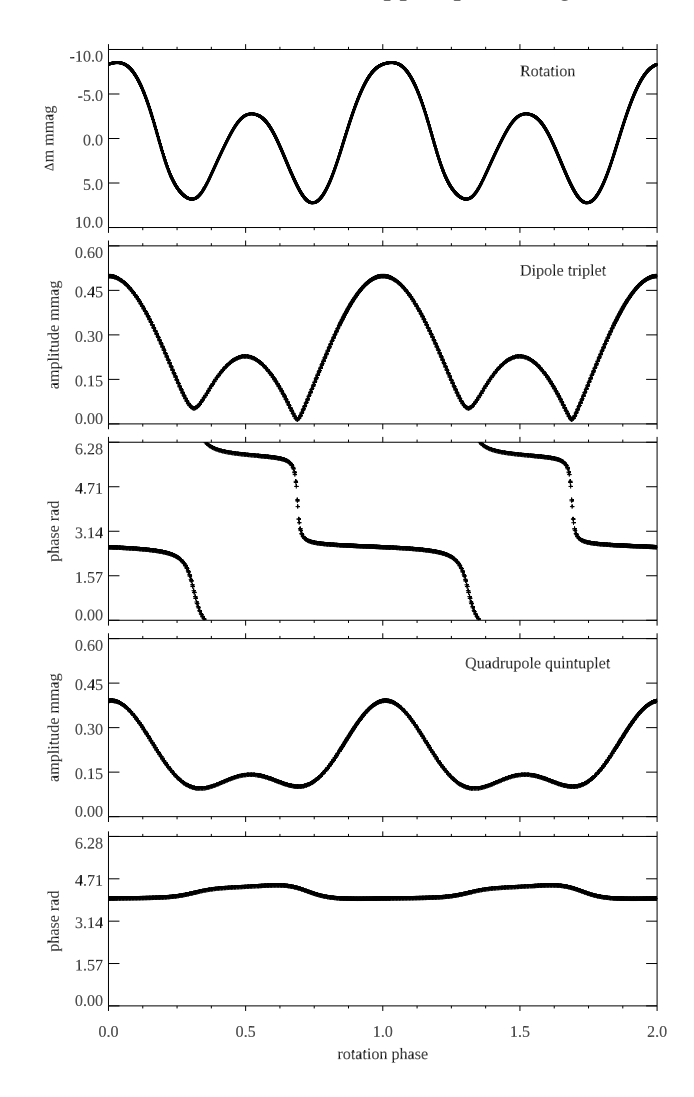


Figure 9. Top panel: The rotation curve. $P_{\rm rot} = 7.679696 \, {\rm d}; t_0 = {\rm BJD} \, 2458500.53070$. Two rotation cycles are shown for visibility across rotation phase zero. Second panel: The pulsation amplitude of the dipole triplet for the S7.1-7.2 JD58497–58510 data. Third panel: The pulsation phase for the dipole triplet. Fourth panel: The pulsation amplitude of the quadrupole quintuplet for the S7.1-7.2 JD58497–58510 data. Bottom panel: The pulsation phase for the quadrupole quintuplet; this has been shifted down by 2 rad for visibility because it wraps around at $2\pi {\rm rad}$. The phase is nearly constant

 $|i+\beta-180|=\alpha=64^\circ$. For a dipole mode the observed amplitude is proportional to $\cos\alpha$ times the intrinsic amplitude. We therefore expect for a pure dipole pulsation that the two pulsation maxima should have an amplitude ratio of $\cos 10^\circ/\cos 64^\circ=2.2$, very close to what is seen in the second panel of Fig. 9.

The quintuplet variations are more complex; this mode is highly distorted. It has a main maximum at rotation phase zero, as does the dipole. With the angle between the pulsation pole and the line of sight being $\alpha=10^\circ$ at this rotation phase, the quadrupole pulsation is dominated by the polar cap, but the equatorial band has some visibility, given that the nodal lines for a zonal quadrupole $(\ell=2,m=0)$ mode are at co-latitude 54.7° from the pulsation pole. At rotation phase 0.5 for the other quadrupole maximum, the equatorial belt is much more prominent. In any case, the nearly constant pulsation phase seen for this mode over the rotation cycle in the bottom panel of Fig. 9 indicates extreme distortion from a

2114 D. W. Kurtz et al.

Table 7. Models of HD 60435 discussed in Section 7. Shown, from top to bottom, are: the model mass, effective temperature, luminosity, age, initial metal mass fraction, and initial helium mass fraction.

	Model a	Model b	Model c
M/M_{\odot}	1.9	1.8	1.6
$T_{\rm eff}$ (K)	7809	7892	7942
L/L_{\odot}	14.48	14.56	14.16
L/L_{\odot} Age (Myr)	745	1072	1224
Z	0.0231	0.0121	0.0071
Y	0.291 91	0.251 92	0.271 92

normal quadrupole mode, with the equatorial belt contributing little to the observed pulsation amplitude. This is seen better in the models below in Section 8.

The amplitude spectra for the half-sectors S13.1 JD58660.80 and S13.2 JD58675.49 also show two triplets (ν_3 and ν_7) and one quintuplet (ν_6). However, those do not completely pre-whiten, so there is some secular amplitude modulation. The quintuplet amplitudes are possibly different to those for S7.1 JD58497.34 and S7.2 JD58510.40 above, so the above discussion of the oblique pulsator model applied to the quadrupole mode may be overinterpreted. Also, the triplet amplitudes for ν_3 give a ratio from equation (6) that differs from that of ν_7 presented about by 2.8σ , another note of caution. The rapid amplitude changes in the modes of this star confound a more precise result.

7 MODE IDENTIFICATION FROM STELLAR MODELLING

The ambiguity in the identification of the degree of the even modes can be addressed by looking at frequency combinations that suppress the dominant large-scale structure in the amplitude spectrum (hereafter, small separations). One such combination that includes dipole and quadrupole modes is (Cunha et al. 2007),

$$\delta_{12}^{1}(\nu) = 2\nu_{n,1} - \nu_{n-1,2} - \nu_{n,2}, \tag{7}$$

or, for dipole and radial modes,

$$\delta_{10}^{1}(\nu) = 2\nu_{n,1} - \nu_{n,0} - \nu_{n+1,0}. \tag{8}$$

High radial order $\ell=2$ and $\ell=0$ modes are expected to have different sensitivities to the innermost layers. Therefore, by comparing the observed small separations with those computed from model frequencies of consecutive $\ell=0,1,0$ and $\ell=2,1,2$ modes, we attempt to identify the degree of the modes observed.

To explore this avenue for mode identification, we consider three different models for HD 60435, with properties listed in Table 7. The models were selected from a set of best fits identified from grid-based modelling following the procedure and model physics described in Deal et al. (2021). Properly accounting for chemical transport in models of Ap stars is a challenge. In the upper atmosphere, the strong magnetic field influences atomic diffusion, with the transport of different elements being impacted differently (Alecian & Stift 2002). Moreover, if working alone, in the interior atomic diffusion would lead to a complete depletion of the photospheric helium and metals (Richer, Michaud & Turcotte 2000). Turbulent mixing, evoked to avoid this depletion when modelling stars more massive than the Sun, is not properly calibrated for Ap stars, whose subphotospheric layers are likely to be significantly affected by the presence of the strong magnetic field.

Acknowledging these limitations to the state-of-the-art, the grid of models constructed by Deal et al. (2021), and used here, does not

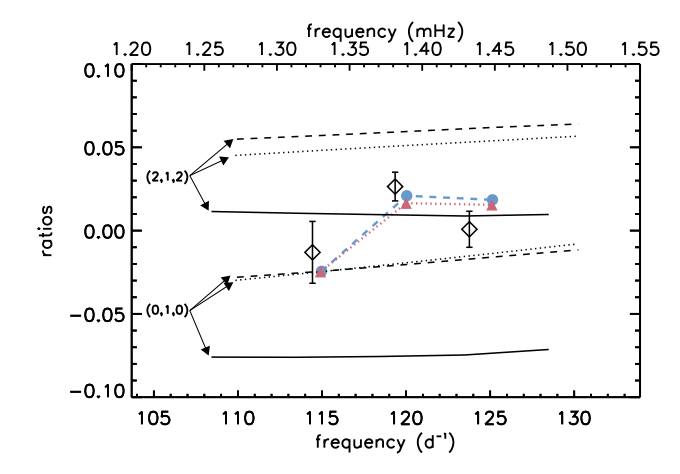


Figure 10. Ratios of small to large frequency separations constructed from the frequencies in Table 2 (open diamonds). Also shown are the ratios computed for the three models listed in Table 7 in the region of the observed frequencies, considering a sequence of alternating even and odd degree modes: model a, high metallicity (black dashed lines); model b, intermediate metallicity (black dotted lines); model c, low metallicity (black dashed—dotted lines). For each model, we show two options for the even modes identified by the arrows: alternating $\ell=0$ and $\ell=1$ modes (0,1,0); alternating $\ell=2$ and $\ell=1$ modes (2,1,2). With filled symbols connected by lines we also identify the ratios obtained by taking the odd modes to be of $\ell=1$, ν_6 to be of $\ell=2$ and ν_1 , ν_4 , and ν_8 to be of $\ell=0$, for model a (circles, blue dashed line) and model b (triangles, red dotted line).

include chemical transport. Since the correspondence between the current surface composition and the initial chemical composition is not possible to achieve based on this grid, no constraints are imposed on the surface metallicity for the identification of the best models. Instead, we select best models with a spread of metallicities. These are derived from exploring the grid, which has a parameter space that includes a significant range of helium and metal mass fractions, without imposing a particular enrichment law (see Deal et al. 2021, for details).

The constraints imposed on the forward modelling were: $T_{\rm eff} = 7900 \pm 200$ K, $L/L_{\odot} = 14.3 \pm 0.7$, and $\Delta \nu \in [51, 58] \, \mu Hz$. From the set of best models retrieved, we chose three representative models covering a range of metallicities. For each of these models we computed the small separations defined by equations (7)–(8). To account for slight differences in the mean density of the models, we further constructed the ratios of small to large frequency separations (Roxburgh & Vorontsov 2003) defined as

$$r_{12} = \frac{\delta_{12}^1}{\nu_{n,2} - \nu_{n-1,2}} \,, \tag{9}$$

and

$$r_{10} = \frac{\delta_{10}^1}{\nu_{n+1,0} - \nu_{n,0}} \,. \tag{10}$$

These model ratios are to be compared with the observed ratios, $r_{\rm obs}$, calculated assuming that ν_3 , ν_5 , and ν_7 are consecutive dipole modes and that ν_1 , ν_4 , ν_6 , and ν_8 are consecutive modes of even degree (note that, the observed ratios do not depend on whether the latter are radial or quadrupole modes).

The results from the data and model comparison can be seen in Fig. 10, with the observed ratios and respective uncertainties shown by open symbols and the model ratios shown by black lines. For all three models, the ratios obtained when considering combinations involving quadrupole modes, hereafter (2,1,2), are

positive, while those obtained for combinations involving radial modes, hereafter (0,1,0), are negative. Moreover, the magnitude of the ratios depends on metallicity, with lower metallicity models having smaller magnitude (2,1,2) ratios and higher magnitude (0,1,0) ratios. This highlights the potential of ratios to identify the even modes, under the assumption that the odd modes are dipolar, and possibly also to constrain the initial chemical composition of roAp stars.

In all cases, Fig. 10 shows that the model ratios computed for sequences of the same alternating even and odd mode degrees vary smoothly with frequency, while the observed ratios apparently do not. However, they are still consistent with a smooth variation within 2σ , in which case the best solution would point to a set of alternating dipolar and quadrupolar modes in a star with a low initial metallicity.

This potential difference between the observations and model results may have different origins. On the one hand, the even degree modes may not all be of the same degree. If we take ν_6 to be a quadrupole (cf. Section 6) and relax the assumption that the observed even modes are all of the same degree, the ratios of high-metallicity and intermediate metallicity models (a and b, respectively) that best represent the data are found when ν_6 is a quadrupole mode and all other even degree modes (i.e. ν_1 , ν_4 , and ν_8) are radial modes. This sequence is shown in Fig. 10 by filled symbols connected by lines in colour for model a (circles, dashed line) and model b (triangles, dotted line) models.

On the other hand, the stellar interior may have regions of sharp stratification, not accounted for in our models, that perturb the ratios away from the smooth frequency behaviour observed in Fig. 10. Regions of strong chemical gradients and transitions between convective and radiative regions are known to induce frequency perturbations that vary cyclically with frequency (see Cunha 2020, for a review). In fact, Vauclair & Théado (2004) argued that chemical transport inside roAp stars could lead to a helium gradient below the convective envelope that, in turn, would result in a non-smooth frequency dependence of particular combinations of the observed frequencies. Depending on the location of these gradients, the ratios computed here could also be affected in a similar way (Deal et al. 2023). Hence, it is possible that the even degree modes are all of the same degree and our models fail to capture the non-smooth dependence of the ratios on frequency because they do not include chemical transport.

7.1 The nature of v_2

In the discussion above we have not considered the nature of ν_2 , the mode that falls off the regular frequency spacing in the amplitude spectrum of HD 60435 (see Fig. 3). Anomalies in otherwise regular frequency spacings have been seen in other multiperiodic roAp stars, such as HD 24712 (HR 1217), for which Cunha (2001) interpreted the anomaly as possibly resulting from the impact of the strong magnetic field on pulsations via the Lorentz force. While generally strong magnetic fields induce frequency perturbations that vary smoothly with radial order, resulting only in a slight increase of the large frequency separation, occasionally a strong disruption of the expected asymptotic regular spacing does occur, similar to what is seen near avoided crossings in evolved solar-like pulsators (Cunha & Gough 2000; Saio & Gautschy 2004; Cunha 2006).

In the present case, if ν_2 results from such an anomaly, then we can interpret it as a dipolar mode. A similar anomaly occurring in the sequence of radial or quadrupole modes would then be expected to take place to the left of ν_2 (i.e. at lower frequencies) where modes are either not driven or do not reach observable amplitudes, such that

the sequences of even and odd modes would remain equally spaced in the observed region.

An alternative explanation to the nature of v_2 is that this is an odd mode of higher degree. Magnetic distortion of the eigenfunctions could give rise to lower degree spherical harmonic components in what would be a higher degree mode, making modes of higher degree potentially easier to observe than in other stellar pulsators (Dziembowski & Goode 1996; Bigot et al. 2000; Cunha & Gough 2000; Saio & Gautschy 2004). This could also explain similar apparent anomalies in other roAp stars.

Inspection of the frequencies of $\ell=3$ modes in the three models listed in Table 7 show that they are separated from the nearest $\ell=1$ mode by ~ 7 to 9 μ Hz, depending on the model, thus are smaller than the nominal measured 12 μ Hz separating ν_2 from ν_3 . Despite this difference, considering that the individual mode frequencies were not used directly as constraints in the model selection, and that the models in Table 6 do not consider the effect of the magnetic field, some caution is called for before rejecting the possibility that ν_2 is an $\ell=3$ mode.

However, the mode of ν_2 presents further challenges to interpretation. It can be seen in Figs 5, 6, A2 and that $\nu_2 = 113.39 \, d^{-1}$ reaches amplitude maximum at a rotation phase of approximately 0.25, i.e. about 90° later in rotation phase to the pulsation maxima of the dipole and quadrupole modes ν_7 and ν_6 . To look at this more carefully, we studied the S6.1–8.1 data (see Table A1 for the dates and durations of these half-sectors) where ν_2 appears to be semi-stable.

We see clear evidence of a frequency triplet in the amplitude spectrum, and find a significant quintuplet split by exactly the rotation frequency by least-squares fitting of the frequencies. We note that the mode frequency is not fully stable over the time-span of the data set used, hence there is significant amplitude remaining after pre-whitening by the quintuplet, making the results less certain. The central frequency of the quintuplet, $113.47\,\mathrm{d}^{-1}$, is the mode frequency. This is a more precise measurement of ν_2 than that given in Table 2 where it was estimated from the centroid of the broad peak from one half-sector when it had good visibility. We then used the frequency quintuplet to generate a plot of pulsation amplitude and pulsation phase as a function of rotational phase, similar to that seen for ν_6 and ν_7 in Fig. 9.

The result for ν_2 is shown in Fig. 11, and it is perplexing. The amplitude reaches maximum near rotation phase 0.25 with a second maximum near rotation phase 0.75. The amplitude variation is not inconsistent with an $\ell=3$ octupole mode with some suppression in the equatorial region, but the rotation phase of pulsation maximum in that case would be 0, not 0.25. We note that the range of pulsation phase change is somewhat less than π rad, but is much less suppressed than for the $\nu_6\ell=2$ quadrupole mode that we show in models in the next section.

We have also considered the possibility of a sectoral dipole mode $(\ell=1,m=|1|)$. For the values of $i=60^\circ$ and $\beta=60^\circ$ – very close to the values that we derived in Section 6 for the ν_7 dipole mode – we calculated the amplitude modulation expected for a zonal dipole mode $(\ell=1,m=0)$ and a sectoral dipole mode $(\ell=1,m=|1|)$. We show these amplitude variations in Fig. 12 where it can be seen that the pure zonal dipole mode amplitude variations are remarkably similar to those observed for ν_7 (see Fig. 9), supporting the identification of that mode, but the amplitude variations for the sectoral dipole mode are not similar to the observations seen in the middle panel of Fig. 11. While both observations and model show an amplitude maximum at rotation phase 0.25, after that they diverge. We dismiss the possibility that the ν_2 mode could be a sectoral dipole mode with the same pulsation axis as the ν_7 mode.

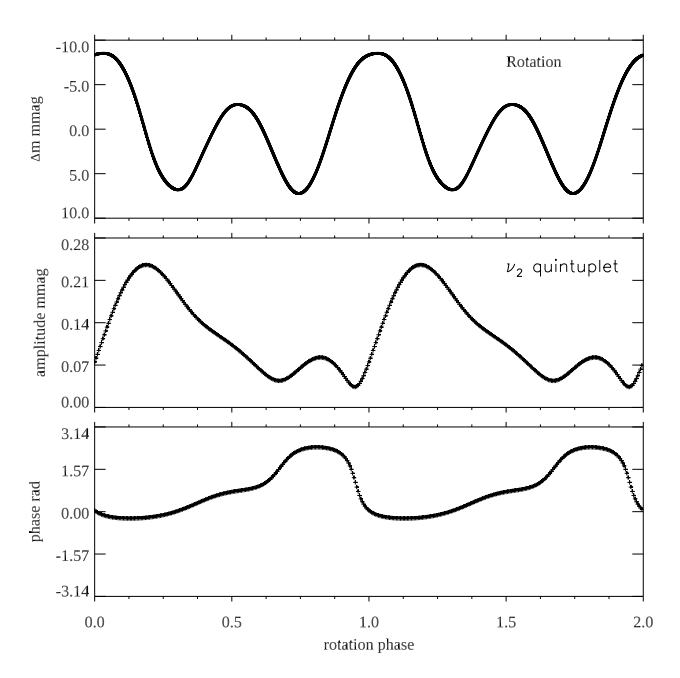


Figure 11. Top panel: The rotation curve (as in Fig. 9) for comparison. Two rotation cycles are shown for visibility across rotation phase zero. Middle and bottom panels: the pulsation amplitude and phase as a function of rotation for the ν_2 mode. The pulsation phase has a zero point shift of π rad for display purposes.

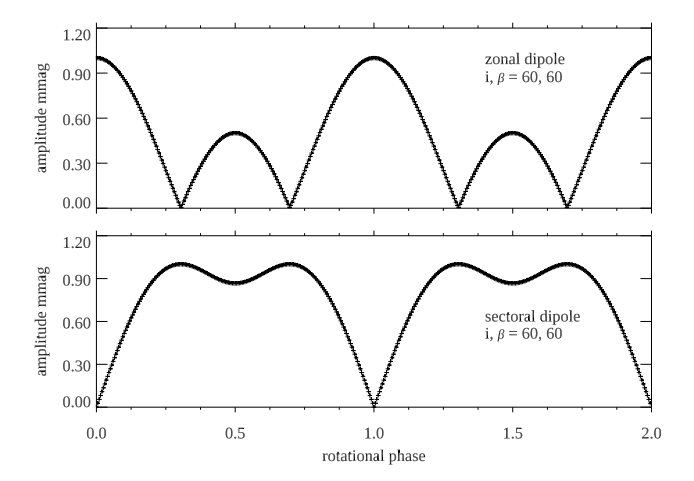


Figure 12. The pulsation amplitude, normalized to 1.0, as a function of rotation phase for top: a zonal dipole mode ($\ell = 1, m = 0$); bottom: a sectoral dipole mode, both with $i = 60^{\circ}$ and $\beta = 60^{\circ}$.

The v_2 mode is reminiscent of those seen in tri-axial tidally tilted pulsators, close binary stars where pulsation modes are excited along three axes, the tidal axis, the orbital/rotation axis, and a third axis orthogonal to both of those (Zhang et al. 2024). This is well understood theoretically (Fuller et al., 2024, in press). The roAp stars may also show modes with different pulsation axes, as a result of the combined effect on pulsations from the magnetic and rotational effects (Bigot & Dziembowski 2002). An example of two modes with different pulsation axes has been reported by Kurtz et al. (2011) for the roAp star KIC 10195926. That this is rarely observed in roAp stars is possibly the consequence of a selective driving of the mode most closely aligned with the magnetic field (Balmforth et al. 2001).

The interpretation of the geometry of the modes in roAp stars is complicated further by the distortion of the modes by the magnetic field, which results in each mode being described by a depth-dependent sum of spherical harmonics of different degree, ℓ (Dziembowski & Goode 1996; Bigot et al. 2000; Cunha & Gough 2000; Saio & Gautschy 2004; Quitral-Manosalva et al. 2018). This could explain why different spectral lines, being sensitive to different atmospheric depths in roAp atmospheres, appear to show different mode geometry when the oblique pulsator model is applied, as reported by Kochukhov (2006) in a spectroscopic line profile study of the roAp star HR 3831. By comparing mode geometries derived from the oblique pulsator model for roAp stars observed in Johnson B and in TESS red filters, Holdsworth et al. (2021) and Kurtz & Holdsworth (2020) also found significant differences in the inferred geometry, depending on the atmospheric depth being sampled through different filters.

Interestingly, in a study of the roAp star HD 12098, Kurtz et al. (2024) found that the single, stable pulsation mode in that star seems to be a dipole mode more distorted than seen in any other star. The pulsation amplitude and phase variations with rotation in HD 12 098 have some similarity to those shown here for ν_2 in HD 60435; they are strongly distorted.

Firm conclusions regarding the interpretation of ν_2 , as well as the identification of the other observed frequencies based on the ratios, as discussed above, require more extensive modelling including the impact of the magnetic field. Such modelling is beyond the purpose of the current paper and shall be performed in future work.

8 MODELS FOR P-MODE PULSATIONS IN THE PRESENCE OF A DIPOLE MAGNETIC FIELD

Rapid oscillations in roAp stars are axisymmetric high-order p mode pulsations with a pulsation axis that is closely aligned to the magnetic axis which is in turn inclined to the rotation axis (Kurtz 1982; Bigot & Kurtz 2011). Strictly speaking, in the presence of a magnetic field, the eigenfunction of an axisymmetric non-radial pulsation mode cannot be represented by a single (m=0) spherical harmonic $Y_l^0(\theta,\phi)$, where (θ,ϕ) are spherical polar co-ordinates with the axis along to the magnetic axis. For this reason, we represent the displacement vector ξ and a perturbed scalar variable f' of an axisymmetric pulsation mode with a sum of terms associated with $Y_\ell^0(\theta,\phi)$ as

$$\boldsymbol{\xi} = \sum_{\ell} \left(\xi_{r\ell} Y_{\ell}^{0} \boldsymbol{e}_{r} + \xi_{h\ell} \frac{\partial Y_{\ell}^{0}}{\partial \theta} \boldsymbol{e}_{\theta} \right), \quad f' = \sum_{\ell} f_{\ell}' Y_{\ell}^{0}. \tag{11}$$

In the couplings with a dipole magnetic field, we have two mutually independent series of modes; even modes (symmetric about the magnetic equator) consist of $\ell=0,2,4,\ldots$, and odd modes consist of $\ell=1,3,5,\ldots$. We also expand the magnetic perturbation B' similarly to ξ . Usually, we include twelve ℓ components for each variable, then we solve 6×12 differential equations with a complex eigenfrequency for non-adiabatic calculations under the Cowling approximation, where the Eulerian perturbation of gravity is neglected (see Saio & Gautschy 2004; Saio 2005, for details). For the representative latitudinal degree ℓ of a mode, we adopt ℓ of the component having the maximum kinetic energy.

The equilibrium stellar model adopted has parameters of $M=1.88\,\mathrm{M}_\odot$, $L=15.25\,\mathrm{L}_\odot$, $T_\mathrm{eff}=7525\,\mathrm{K}$, and $R=2.30\,\mathrm{R}_\odot$. The model was taken from the evolution model with a central hydrogen abundance of 0.28, and was chosen for the large frequency separation to be $\approx 51\,\mathrm{\mu Hz}$ at $B_\mathrm{p}=0$ and global parameters not far from the estimates discussed in Section 6. This model has an abundance of

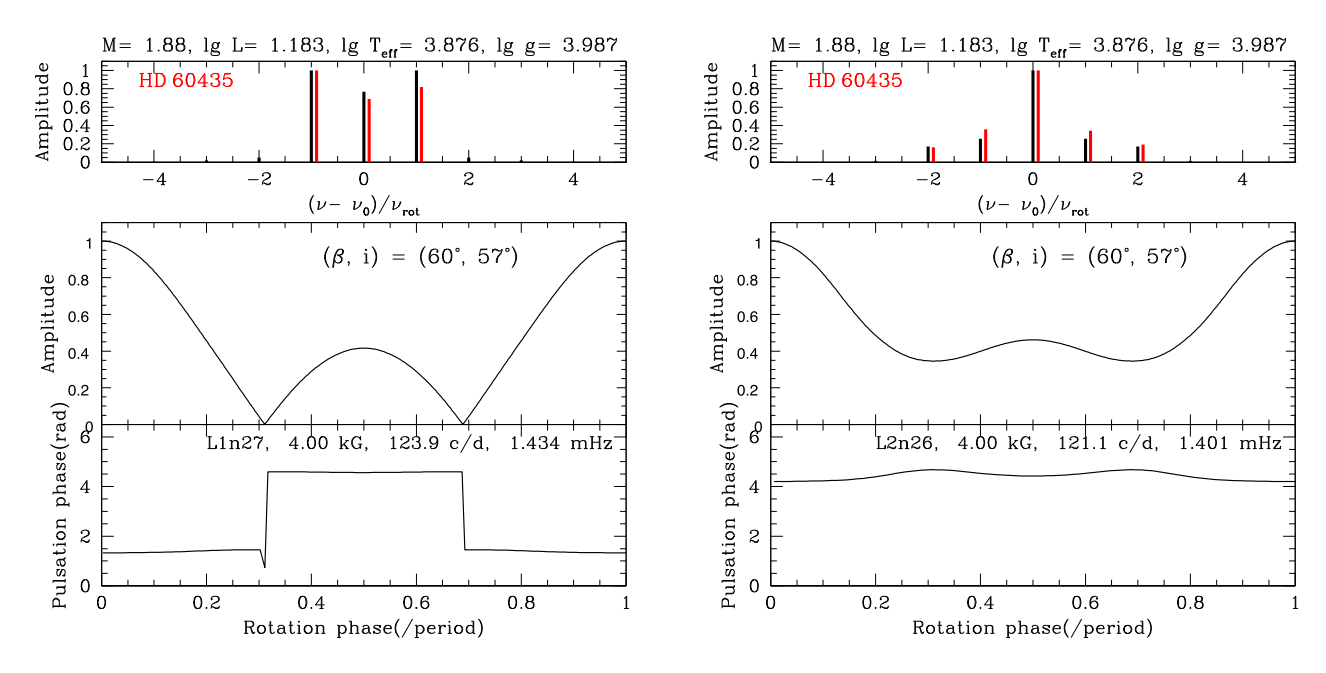


Figure 13. Models for pulsation amplitude (middle panels) and phase (bottom panels) modulations for the deformed dipole mode of v_7 (left panel) and the deformed quadrupole mode of v_6 (right panel). The top panels show the amplitudes of the pulsation and rotation sidelobes (normalized to unity at maximum) for the corresponding pulsations; red and black lines are, respectively, observed amplitudes of HD 60435 and model predictions at $B_p = 4 \,\mathrm{kG}$.

heavy elements Z = 0.02, but helium is assumed to be depleted to $Y_s = 0.01$ above the He II ionization zone, and convection in the envelope to be suppressed, assuming a strong magnetic field to stabilize the outer layers (polar model of Balmforth et al. 2001).

The eight frequencies observed for HD 60435 approximately agree with three dipole modes, four $\ell=2$ modes, and an $\ell=3$ mode of the model at $B_{\rm p}\approx 4\,{\rm kG}$. The magnetic field strength is consistent with the estimate discussed in Section 4 based on the longitudinal magnetic field observed by Hubrig et al. (2006). We have obtained amplitude and phase modulations using the method discussed in Saio & Gautschy (2004) for $\ell=1$ and 2 modes close to ν_7 and ν_6 at $B_{\rm p}=4\,{\rm kG}$ to compare with the observed ones shown in Fig. 8. The results of our model are shown in Fig. 13, where we adopted a rotational inclination angle $i=57^\circ$ derived from the radius of our model, $2.30\,{\rm R}_\odot$, with the rotation period and $\nu\sin i$ of HD 60435 determined in this paper and $\beta=60^\circ$ then derived from equation (6). We note that the adopted i and β are within the uncertainties discussed in Section 7.

The phase modulation of the distorted $\ell=2$ mode ν_6 is strongly suppressed in accordance with our model. Such suppressions are known to occur in other roAp stars (e.g. Holdsworth et al. 2018a, b).

9 DISCUSSION AND CONCLUSIONS

It is known that modes in stochastically driven pulsators – solar-like and red giant oscillators – have short lifetimes, hence show strong amplitude modulation. This is unsurprising, given the non-periodic nature of the driving. It is also known that heat-engine pulsators – those driven by the κ -mechanism – often show amplitude modulation on a variety of time-scales. Examples of this for Polaris, Deneb, Spica, and white dwarfs were discussed in the introduction, Section 1. While the physical conditions and processes governing pulsation amplitude stability in these stars are expected to be different to those in main sequence pulsators, the phenomenological similarity between these objects is striking. In some heat engine driven pulsators, some modes have been observed to appear, and to

disappear. But in no previous case has a pulsating star been observed to cease all pulsations, as has the roAp star HD 60435.

We know that HD 60435 was pulsating when it was observed in 1983 (Kurtz 1984; Johnson *B*), 1984 (Matthews et al. 1986; Johnson B), 1985 (Matthews et al. 1987; Johnson B), 1991 (Taylor et al. 1993; HST UV), 2014 (this paper, radial velocities), and from 2018 September to 2020 October (TESS red bandpass), after which the pulsation stopped, at least up to the last TESS (as of this writing) observations in 2023 September, and the LCOGT ground-based observations in 2024 January. We do not know if it had observable pulsations at the times when it was not observed; the largest gap in the observing record is 13 yr. But other roAp stars have shown nearly stable pulsations over decades. There has never been any reason to suspect that an roAp star - or any other pulsator - could cease pulsating on a time-scale far shorter than an evolutionary time. Thus, the primary result of this paper is that HD 60435 stopped pulsating. It is not understood why, so we now make some conjectures on the implications of this.

Figs 4, 5, and 6 and A1 and A2 suggest that when modes near ν_4 are strong, modes ν_2 , ν_6 , and ν_7 are weak, and vice versa. These modes look to be coupled and exchanging energy. Non-linear mode coupling among observed modes and other modes that are of too high a degree to be observed has been proposed by Dziembowski & Krolikowska (1985) and discussed by Bowman et al. (2016) as a possible explanation for amplitude variability among 983 δ Sct stars observed by *Kepler*. This requires a tight resonance among 'parent' and 'child' mode frequencies, which seems possible for δ Sct stars where only a few of many modes show amplitude modulation, and the frequency spectrum is densely populated with mode frequencies in models.

This could also be an explanation for the disappearance of observable pulsation in HD 60435, i.e. the observed modes coupled with, and transferred their pulsation energy to, higher degree modes that do not produce observable light variations. It would require that all observed mode frequencies – not just some as in δ Sct stars – coupled resonantly with higher degree, unobservable mode

frequencies. That is more challenging to accept than the case for δ Sct stars with only a few resonances generating amplitude modulation. We see no way at present to test this conjecture.

An alternative is that in the balance between the pulsation driving and the global damping of the modes, damping won (i.e. the linear growths rates became negative). This is what must happen when stars evolve out of instability regions, so can we conjecture that we have just caught HD 60435 evolving out of the roAp instability region? Given its $T_{\rm eff}$ and L, that is unlikely, but if that conjecture were correct, then we can predict that HD 60435 will not be observed to pulsate in future observations. That is falsifiable if the pulsations return. Future observations are planned to test this conjecture. Alternatively, can pulsations just stop for reasons other than evolutionary changes in the stellar structure on a time-scale of weeks for HD 60435? That would require a very fine balance between the driving and damping, and then a subtle change in the star to tip the balance. At present, we have no models with sufficient confidence to address this question. Note, for example, that the modes in HD 60435 are theoretically not driven at all in the model we presented in Section 9.

There is the further question of why we do not see in the TESS data the long series of frequencies between 0.7-1.3 mHz found by Matthews et al. (1987) and listed in Table 2. Were those frequencies actually present in the 1984-1985 data? If so, those modes had stopped pulsating by the time of the TESS observations. Or, were the challenges of signal-to-noise and complex spectral windows in the ground-based data such that those frequency identifications were not secure? Those ground-based data were obtained from Cerro Tololo InterAmerican Observatory (CTIO), Las Campanas Observatory (LCO) and the South African Astronomical Observatory (SAAO) contemporaneously, but the lower frequencies identified are only visible in the LCO data, hence perhaps were an artefact. Should they reappear in future observations, then their reality will be proved. But should they not be observed again, no further conclusion can be drawn, since we know HD 60435 is capable of stopping pulsating.

The ceasing of pulsations in HD 60435 has an impact on the question of why only 5.5 per cent of magnetic Ap stars are roAp stars (Holdsworth et al. 2024), the rest being labelled as noAp (non-oscillating Ap) stars. Since we now have this one case of an roAp star becoming an noAp star in a matter of weeks, the distinction between roAp and noAp is blurred.

This problem is more general. For example, Gootkin et al. (2024) examined millions of light curves in TESS 30-min cadence data and found that out of nearly 16 000 δ Sct stars the pulsator fraction peaks at 50–70 per cent in the centre of the δ Sct instability strip. They found a correlation between pulsator fraction and rotation, hence deduced that rotation plays a role in driving in δ Sct stars. Murphy et al. (2024) showed that the δ Sct pulsator fraction is also dependent on age, even for stars that remain inside the instability strip. The general question is why do some stars in an instability strip pulsate while others do not, when the stars may share T_{eff} , L, age, [Fe/H], binarity. What are the additional factors that govern this? For the δ Sct stars, Gootkin et al. showed rotation is one such factor. But for the roAp stars, we do not know what the factors are that select between roAp and noAp, although it does not appear to be rotation, as the vast majority of Ap stars are relatively slow rotators with periods between 1–10 d (Wraight et al. 2012; Labadie-Bartz et al. 2023), and some are super-slowly rotating with periods up to centuries (Mathys, Holdsworth & Kurtz 2024). The cessation of pulsation in HD 60435 highlights that this important question needs more work.

In addition to the major conclusion of this paper that HD 60435 stopped pulsating, with all of the implication of that, we have also learned more from this star. Since it showed stable pulsations for more than a rotation period, we were able to apply the oblique pulsator model and extract constraints on the geometry of the pulsation modes, i.e. constrain the rotational inclination, i, and the pulsation axis (hence the magnetic axis) obliquity, β . We showed that the magnetic pulsation model of Saio (2005) inferred a polar magnetic field strength of 4kG, in good agreement with the one magnetic observation that has been published. This reinforces confidence in the theory for that model, which explains the suppression of pulsation amplitude in the pulsational equatorial zone for quadrupole modes, thus the small changes in pulsation phase for a quadrupole mode with the rotation of the star. Thus, HD 60435 joins a small number of roAp stars for which this phase suppression in obliquely pulsating quadrupole modes has been observed (e.g. Holdsworth et al. 2018a, b).

Using the models of Deal et al. (2021), we examined the frequency spacing in HD 60435 to address two issues: the degree of the even modes, and the degree and frequency spacing of the ν_2 mode. We found that ν_6 is a quadrupole mode, but that the other even degree modes could be either quadrupole or radial modes, depending on the metallicity of the star. This highlights the potential of the frequency spacings in roAp stars to constrain the global metallicity, something that cannot be done by spectroscopy because of the extreme atmospheric abundance anomalies in Ap stars.

While identification of the degree of the ν_2 mode awaits future modelling, from the frequency spacing, it is potentially a highly distorted octupole ($\ell=3$) mode with strong suppression of the pulsation in the equatorial band making the mode visible. If so, HD 60435 highlights opportunities for asteroseismic constraints with higher degree modes than the $\ell=1,2$ that have previously been identified and modelled in roAp stars.

ACKNOWLEDGEMENTS

We thank Morgan Deal for providing the information on the models considered in Section 7. We thank Barry Smalley for providing a determination of $T_{\rm eff}$ from the IRFM. We thank Guy Davies and David Mkrtichian for useful discussions on HD 60435. This work has been partially supported by Fundação pa a Ciência e Tecnologia FCT-MCTES, Portugal, through national funds by these grants: DOI: 10.54499/UIDB/04434/2020; DOI: 10.54499/UIDP/04434/2020 and DOI:10.54499/2022.03993.PTDC. MC is funded by FCT-MCTES by the contract with reference CEECIND/02619/2017. GH thanks the Polish National Center for Science (NCN) for supporting this study through grant 2021/43/B/ST9/02972. SJM is supported by the Australian Research Council through Future Fellowship FT210100485. Co-funded by the European Union (ERC, MAGNIFY, Project 101126182). Views and opinions expressed are however those of the authors only and do not necessarily reflect those of the European Union or the European Research Council. Neither the European Union nor the granting authority can be held responsible for them. This paper includes data collected by the TESS mission. Funding for TESS is provided by NASA's Science Mission Directorate. Resources used in this work were provided by the NASA High End Computing (HEC) Program through the NASA Advanced Supercomputing (NAS) Division at Ames Research Center for the production of the SPOC data products. Based in part on data acquired at the Anglo-Australian Telescope, under programs A/2024A/016 and A/2024B/011. We acknowledge the traditional custodians of the

land on which the AAT stands, the Gamilaraay people, and pay our respects to elders past and present. Some of the observations reported in this paper were obtained with the Southern African Large Telescope (SALT). This work made use of observations from the Las Cumbres Observatory global telescope network. This work has made use of data from the European Space Agency (ESA) mission *Gaia* (https://www.cosmos.esa.int/gaia), processed by the *Gaia* Data Processing and Analysis Consortium (DPAC, https://www.cosmos.esa.int/web/gaia/dpac/consortium). Funding for the DPAChas been provided by national institutions, in particular the institutionsparticipating in the *Gaia* Multilateral Agreement. This work made use of Astropy, a community-developed core Python package and an ecosystem of tools and resources for astronomy.

DATA AVAILABILITY

The *TESS* data used in this study are available on MAST. The SALT spectra are available from the SALT data archive: https://ssda.saao.ac.za. The ground-based data from Matthews et al. (1987) are available from DWK on request. The AAT spectra are available from the AAT archive,³ or from SJM on request.

REFERENCES

Abt H. A., Guzik J. A., Jackiewicz J., 2023, PASP, 135, 124201

Aerts C., 2021, Rev. Mod. Phys., 93, 015001

Aerts C., de Pauw M., Waelkens C., 1992, A&A, 266, 294

Aerts C., Christensen-Dalsgaard J., Kurtz D. W., 2010, Asteroseismology (Astronomy and Astrophysics Library). Springer, Dordrecht

Alecian G., Stift M. J., 2002, A&A, 387, 271

Astropy Collaboration, 2022, ApJ, 935, 167

Balmforth N. J., Cunha M. S., Dolez N., Gough D. O., Vauclair S., 2001, MNRAS, 323, 362

Balona L. A., Holdsworth D. L., Cunha M. S., 2019, MNRAS, 487, 2117

Bigot L., Dziembowski W. A., 2002, A&A, 391, 235

Bigot L., Kurtz D. W., 2011, A&A, 536, A73

Bigot L., Provost J., Berthomieu G., Dziembowski W. A., Goode P. R., 2000, A&A, 356, 218

Blanco-Cuaresma S., 2019, MNRAS, 486, 2075

Blanco-Cuaresma S., Soubiran C., Heiter U., Jofré P., 2014, A&A, 569, A111

Bowman D. M., Holdsworth D. L., 2019, A&A, 629, A21

Bowman D. M., Kurtz D. W., 2014, MNRAS, 444, 1909

Bowman D. M., Kurtz D. W., Breger M., Murphy S. J., Holdsworth D. L., 2016, MNRAS, 460, 1970

Bramall D. G. et al., 2010, in McLean I. S., Ramsay S. K., Takami H., eds, Proc. SPIE Conf. Ser. Vol. 7735, Ground-based and Airborne Instrumentation for Astronomy III. SPIE, Bellingham, p. 77354F

Breger M., 2000, MNRAS, 313, 129

Breger M., Montgomery M. H., Lenz P., Pamyatnykh A. A., 2017, A&A, 599, A116

Brown T. M. et al., 2013, PASP, 125, 1031

Bruntt H. et al., 2008, ApJ, 683, 433

Buckley D. A. H., Swart G. P., Meiring J. G., 2006, in Stepp L. M., ed., Proc. SPIE Conf. Ser. Vol. 6267, Ground-based and Airborne Telescopes. SPIE, Bellingam, p. 62670Z

Cannon A. J., Pickering E. C., 1993, VizieR Online Data Catalog: Henry Draper Catalogue and Extension (Cannon + 1918–1924; ADC 1989).
 VizieR On-line Data Catalog: III/135A. Originally published in: Harv. Ann. 91–100 (1918–1924)

Carrell K. et al., 2024, ApJ, 973, 157

Chapellier E., Valtier J. C., Sareyan J. P., Le Contel J. M., Ducatel D., Morel P. J., 1985, A&A, 143, 466 Crause L. A. et al., 2014, in Ramsay S. K., McLean I. S., Takami H., eds, Proc. SPIE Conv. Ser. Vol. 9147, Ground-based and Airborne Instrumentation for Astronomy V. SPIE, Bellingham, p. 91476T

Creevey O. L. et al., 2023, A&A, 674, A26

Cunha M. S., 2001, MNRAS, 325, 373

Cunha M. S., 2006, MNRAS, 365, 153

Cunha M. S., 2020, in Monteiro M. J. P. F. G., García R. A., Christensen-Dalsgaard J., McIntosh S. W., eds, Astrophysics and Space Science Proc. Vol. 57, Dynamics of the Sun and Stars; Honoring the Life and Work of Michael J. Thompson. Springer International Publishing, Cham, p. 185

Cunha M. S., Gough D., 2000, MNRAS, 319, 1020

Cunha M. S. et al., 2007, A&A Rev., 14, 217

Cunha M. S. et al., 2019, MNRAS, 487, 3523

Deal M., Cunha M. S., Keszthelyi Z., Perraut K., Holdsworth D. L., 2021, A&A, 650, A125

Deal M. et al., 2023, A&A, 673, A49

Desmet M. et al., 2009, Commun. Asteroseismology, 158, 303

Dinshaw N., Matthews J. M., Walker G. A. H., Hill G. M., 1989, AJ, 98, 2249

Donati J. F., Collier Cameron A., 1997, MNRAS, 291, 1

Dziembowski W. A., Goode P. R., 1996, ApJ, 458, 338

Dziembowski W., Krolikowska M., 1985, AcA, 35, 5

Elkin V. G., Kurtz D. W., Mathys G., 2005, MNRAS, 364, 864

Fouesneau M. et al., 2023, A&A, 674, A28

Gaia Collaboration et al., 2016a, A&A, 595, A1

Gaia Collaboration et al., 2023a, A&A, 674, A1

Gilbert J. et al., 2018, in Evans C. J., Simard L., Takami H., eds, Proc. SPIE Conf. Ser. Vol. 10702Y, Ground-based and Airborne Instrumentation for Astronomy VII. SPIE, Bellingham, p. 107020Y

Gootkin K., Hon M., Huber D., Hey D. R., Bedding T. R., Murphy S. J., 2024, ApJ, 972, 137

Guzik J. A., Kloppenborg B., Jackiewicz J., 2024, preprint (arXiv:2410.23985)

Handler G., WET Network of Collaborators, 2013, in Krzesiński J., Stachowski G., Moskalik P., Bajan K., eds, ASP Conf. Ser. Vol. 469, 18th European White Dwarf Workshop. Astron. Soc. Pac., San Francisco, p. 53

Holdsworth D. L. et al., 2018a, MNRAS, 473, 91

Holdsworth D. L., Saio H., Bowman D. M., Kurtz D. W., Sefako R. R., Joyce M., Lambert T., Smalley B., 2018b, MNRAS, 476, 601

Holdsworth D. L. et al., 2021, MNRAS, 506, 1073

Holdsworth D. L. et al., 2024, MNRAS, 527, 9548

Houdebine E. R., 2011, MNRAS, 416, 2233

Houk N., Cowley A. P., 1975, University of Michigan Catalogue of two-Dimensional Spectral Types for the HD stars, Vol. I. Declinations -90_ to -53. University of Michigan, Ann Arbor, MI

Hubrig S., North P., Schöller M., Mathys G., 2006, Astron. Nachr., 327, 289

Kepler S. O. et al., 2003, A&A, 401, 639

Kniazev A. Y., Gvaramadze V. V., Berdnikov L. N., 2016, MNRAS, 459, 3068

Kniazev A. Y., Gvaramadze V. V., Berdnikov L. N., 2017, in Balega Y. Y., Kudryavtsev D. O., Romanyuk I. I., Yakunin I. A., eds, ASP Conf. Ser. Vol. 510, Stars: From Collapse to Collapse. Astron. Soc. Pac., San Francisco, p. 480

Kochukhov O., 2006, A&A, 446, 1051

Kupka F., Dubernet M. L., VAMDC Collaboration, 2011, Balt. Astron., 20, 503

Kurtz D. W., 1982, MNRAS, 200, 807

Kurtz D. W., 1984, MNRAS, 209, 841

Kurtz D. W., 1985, MNRAS, 213, 773

Kurtz D. W., 2022, ARA&A, 60, 31

Kurtz D. W., Holdsworth D. L., 2020, Astrophys. Space Sci. Proc., 57, 313

Kurtz D. W., van Wyk F., Marang F., 1990, MNRAS, 243, 289

Kurtz D. W. et al., 2011, MNRAS, 414, 2550

Kurtz D. W., Saio H., Holdsworth D. L., Joshi S., Seetha S., 2024, MNRAS, 529, 556

³https://archives.datacentral.org.au/query

Labadie-Bartz J., Hümmerich S., Bernhard K., Paunzen E., Shultz M. E., 2023, A&A, 676, A55

Lomb N. R., 1978, MNRAS, 185, 325

Loumos G. L., Deeming T. J., 1978, Ap&SS, 56, 285

Mathys G., Holdsworth D. L., Kurtz D. W., 2024, A&A, 683, A227

Matthews J. M., Kurtz D. W., Wehlau W. H., 1986, ApJ, 300, 348

Matthews J. M., Kurtz D. W., Wehlau W. H., 1987, ApJ, 313, 782

Medupe R., Kurtz D. W., Elkin V. G., Mguda Z., Mathys G., 2015, MNRAS, 446, 1347

Montgomery M. H., O'Donoghue D., 1999, Delta Scuti Star Newslett., 13, 28

Murphy S. J., Grigahcène A., Niemczura E., Kurtz D. W., Uytterhoeven K., 2012, MNRAS, 427, 1418

Murphy S. J., Bedding T. R., Gautam A., Kerr R. P., Mani P., 2024, MNRAS, 534, 3022

Preston G. W., 1967, ApJ, 150, 547

Quitral-Manosalva P., Cunha M. S., Kochukhov O., 2018, MNRAS, 480, 1676

Richer J., Michaud G., Turcotte S., 2000, ApJ, 529, 338

Ricker G. R. et al., 2015, J. Astron. Telesc. Instrum. Syst., 1, 014003

Roxburgh I. W., Vorontsov S. V., 2003, A&A, 411, 215

Różański T., Niemczura E., Lemiesz J., Posiłek N., Różański P., 2022, A&A, 659, A199

Ryabchikova T., Sachkov M., Kochukhov O., Lyashko D., 2007, A&A, 473, 907

Saio H., 2005, MNRAS, 360, 1022

Saio H., Gautschy A., 2004, MNRAS, 350, 485

Schöller M., Correia S., Hubrig S., Kurtz D. W., 2012, A&A, 545, A38

Stibbs D. W. N., 1950, MNRAS, 110, 395

Taylor M., Nelson M. J., Bless R. C., Dolan J. F., Elliot J. L., Percival J. W., Robinson E. L., van Citters G. W., 1993, ApJ, 413, L125

Tkachenko A. et al., 2016, MNRAS, 458, 1964

Turner D. G., Savoy J., Derrah J., Abdel-Sabour Abdel-Latif M., Berdnikov L. N., 2005, PASP, 117, 207

Vauclair S., Théado S., 2004, A&A, 425, 179

Wraight K. T., Fossati L., Netopil M., Paunzen E., Rode-Paunzen M., Bewsher D., Norton A. J., White G. J., 2012, MNRAS, 420, 757

Wright D. J., 2008, PhD thesis, University of Canterbury

Yang T.-Z., Zuo Z.-Y., Sun X.-Y., Tang R.-X., Esamdin A., 2022, ApJ, 936, 48

Zhang V., Rappaport S., Jayaraman R., Kurtz D. W., Handler G., Fuller J., Borkovits T., 2024, MNRAS, 528, 3378

Zverko J., Ziznovsky J., North P., 1998, Contrib. Astron. Obs. Skalnate Pleso, 28, 109

APPENDIX A: THE HALF-SECTOR INFORMATION AND PLOTS

Table A1. Times and durations of the *TESS* half-sectors and full sectors. The data half-sectors are also named with the mid-time of each half-sector for further identification of the individual amplitude spectra in Figs 4 and A1, and to judge the time distributions. Columns 5 and 6 give, respectively, the duration of the half-sectors and their combined sector in days. All the data are 120-s cadence, except S61, 62, 63, and 67, which are 200-s cadence.

TESS Sector	Data set name	BJD time start	BJD time end	Duration	days
		2400	000+	half sector	full sector
3.1	JD58390.03	58 385.934 815	58 394.154 367	8.22	
3.2	JD58401.42	58 396.639 116	58 406.212 895	9.57	20.28
6.1	JD58472.65	58 468.272 565	58 477.021 355	8.75	
6.2	JD58484.18	58 478.243 596	58 490.045 204	11.80	21.77
7.1	JD58497.34	58 491.634 114	58 503.038 448	11.40	
7.2	JD58510.40	58 504.710 685	58 516.087 190	11.38	24.45
8.1	JD58523.56	58 517.984 416	58 529.066 416	11.08	
8.2	JD58539.01	58 536.019 205	58 542.001 135	5.98	24.02
9.1	JD58549.94	58 544.327 512	58 555.542 723	11.22	
9.2	JD58563.02	58 557.571 871	58 568.475 921	10.90	24.15
10.1	JD58576.50	58 571.218 945	58 581.785 451	10.57	
10.2	JD58590.40	58 585.104 836	58 595.681 025	10.58	24.46
13.1	JD58660.80	58 653.919 997	58 667.689 174	13.77	
13.2	JD58675.49	58 668.623 876	58 682.355 603	13.73	28.44
27.1	JD59041.26	59 036.277 847	59 046.545 744	10.27	
27.2	JD59053.87	59 049.152 647	59 058.588 651	9.44	22.31
30.1	JD59121.35	59 115.884 497	59 126.794 366	10.91	
30.2	JD59135.83	59 130.208 301	59 141.441 833	11.23	25.56
33.1	JD59207.80	59 201.733 424	59 213.864 218	12.13	
33.2	JD59221.50	59 215.435 079	59 227.572 775	12.14	25.84
34.1	JD59234.95	59 229.000 568	59 240.906 264	11.91	
34.2	JD59248.20	59 242.357 667	59 254.066 081	11.71	25.07
35.1	JD59260.96	59 255.814 700	59 266.110 553	10.30	
35.2	JD59276.00	59 272.013 326	59 279.979 952	7.97	24.17
37.1	JD59313.64	59 308.254 647	59 319.030 847	10.78	
37.2	JD59327.00	59 321.412 748	59 332.579 186	11.17	24.32
61.1	JD59969.00	59 962.796 133	59 975.196 726	12.40	
61.2	JD59981.82	59 975.412 006	59 988.224 578	12.81	25.43
62.1	JD59994.68	59 988.439 857	60 000.923 658	12.48	
62.2	JD60007.65	60 001.136 621	60 014.152 763	13.02	25.71
63.1	JD60020.88	60 014.368 039	60 027.391 059	13.02	
63.2	JD60034.25	60 027.604 019	60 040.897 809	13.29	26.53
67.1	JD60133.44	60 126.639 041	60 140.247 607	13.61	
67.2	JD60147.43	60 140.460 567	60 154.393 260	13.93	27.75
68.1	JD60160.23	60 154.910 362	60 165.607 499	10.70	
68.2	JD60173.98	60 168.485 256	60 179.510 225	11.02	24.60
69.1	JD60187.58	60 182.353 276	60 192.596 356	10.24	
69.2	JD60200.70	60 195.396 365	60 206.035 332	10.64	23.68

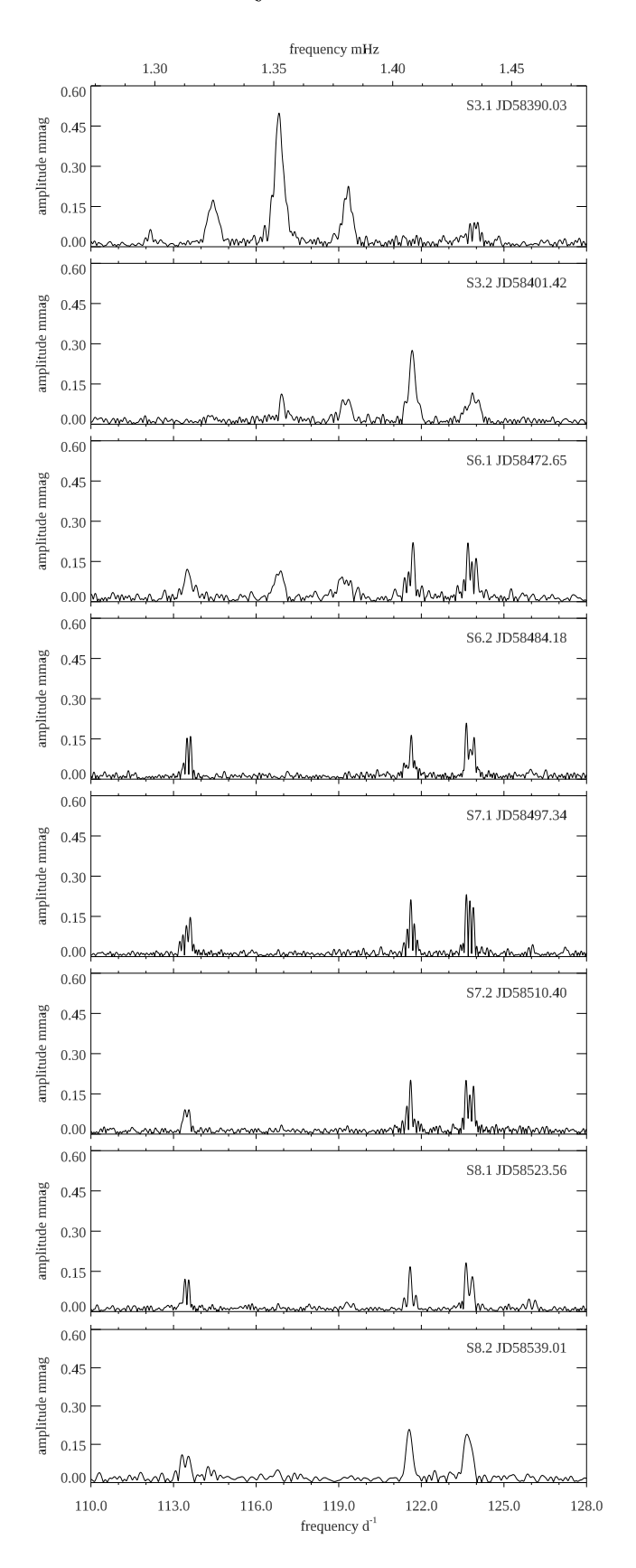


Figure A1. Amplitude spectra of the half-sectors showing the amplitude modulation and mode changes. Note the ordinate scale changes for S10.2 JD58590.40 and S27.1 JD59041.26.

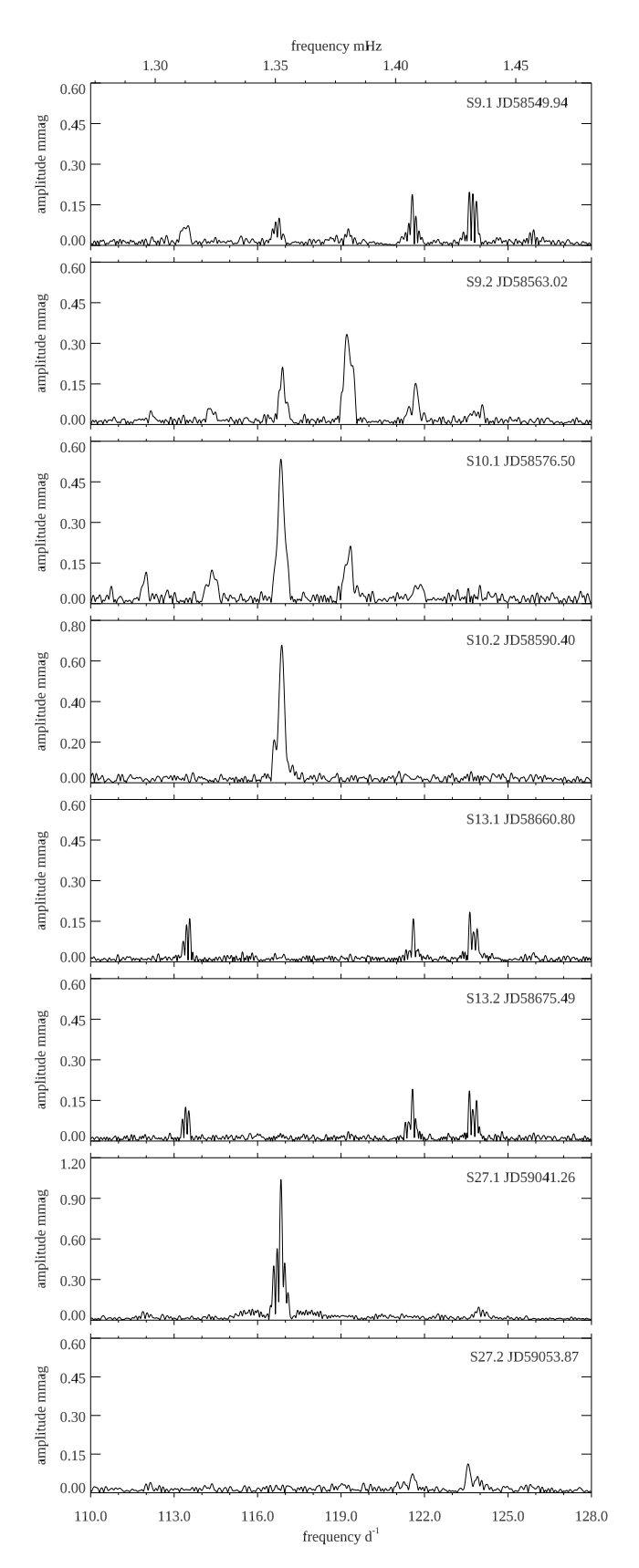


Figure A1. - continued

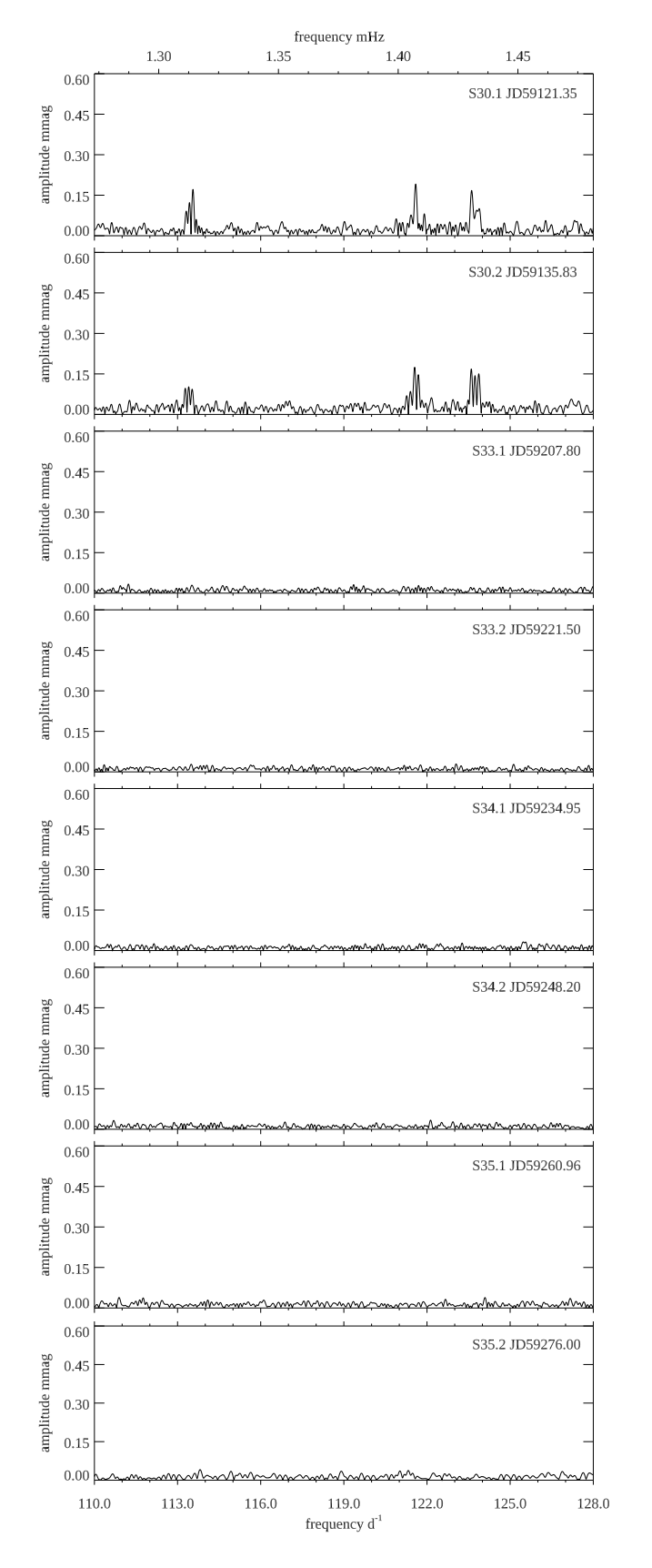


Figure A1. - continued

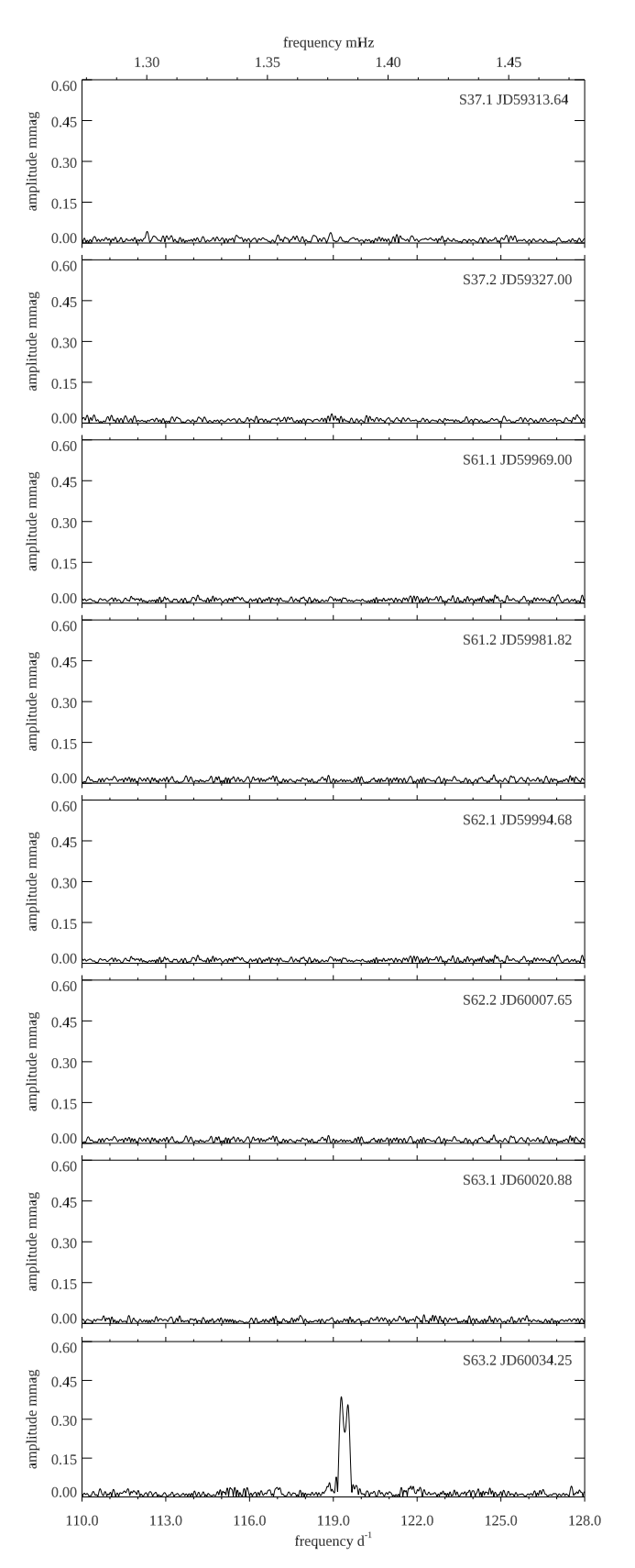


Figure A1. - continued

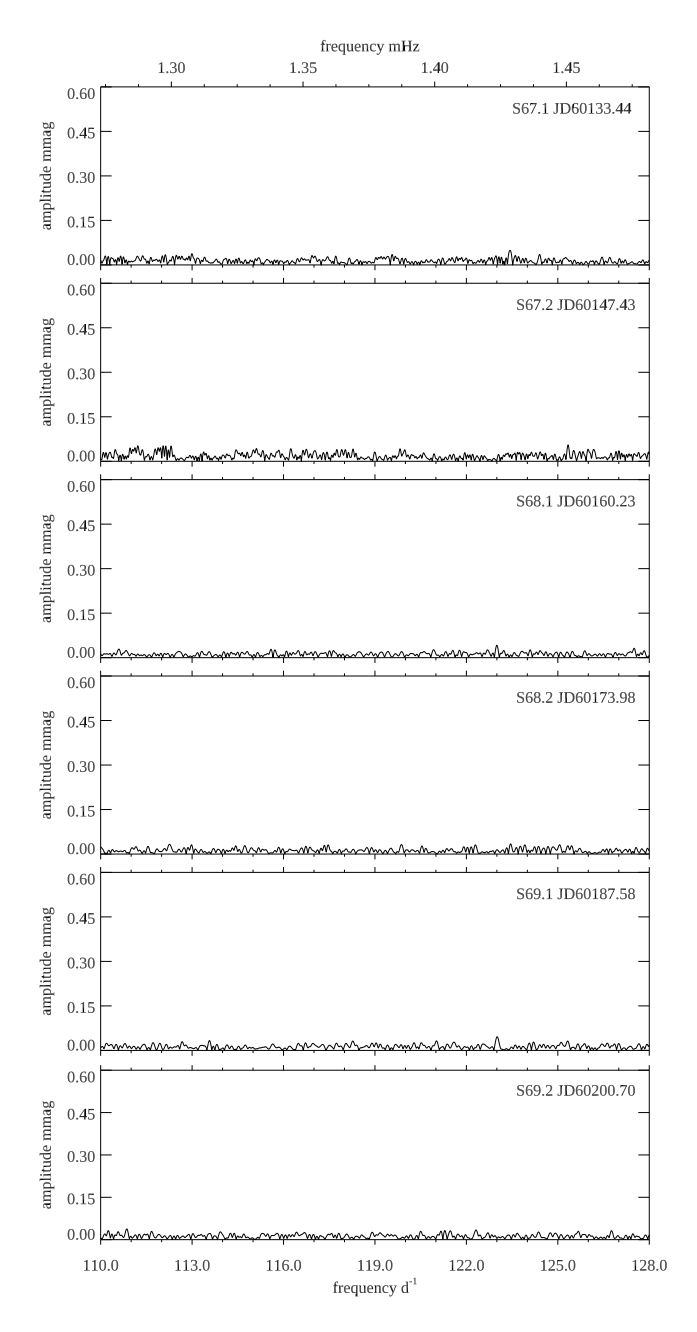


Figure A1. - continued

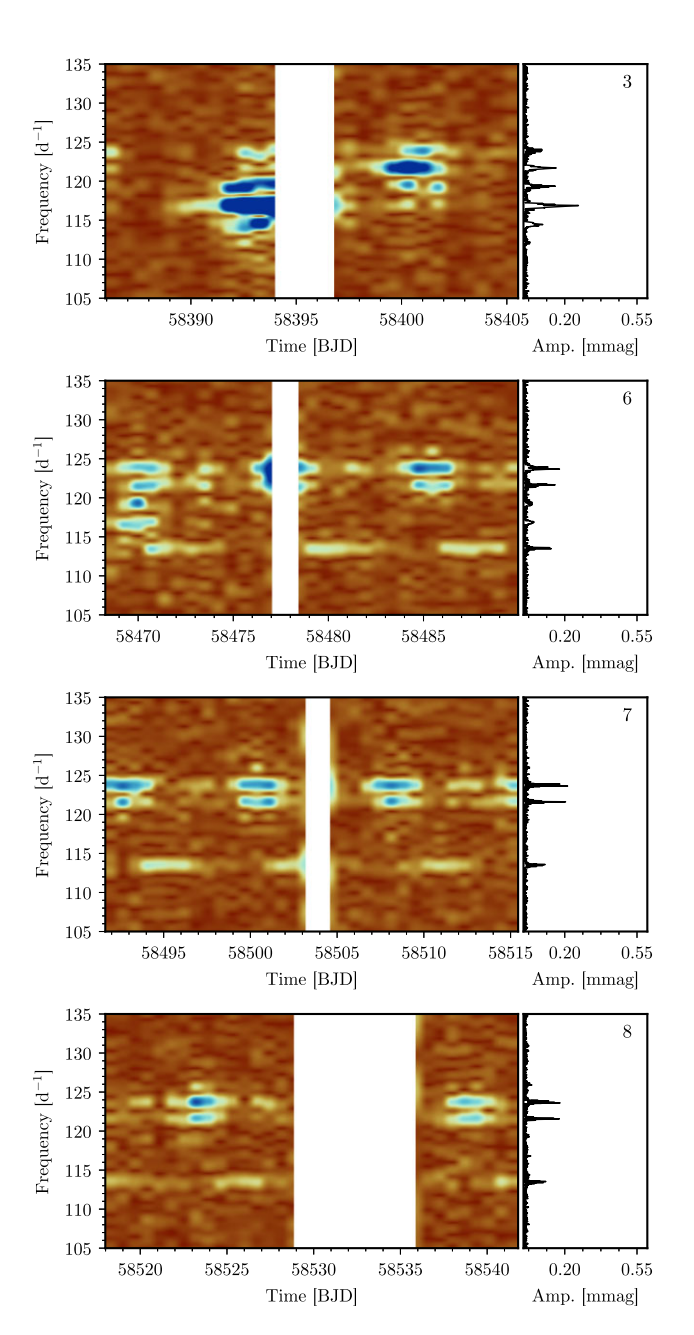


Figure A2. Wavelet plots by sector. The time is BJD -2400000. The amplitude modulations from both the changing view of oblique pulsation with the 7.679696-d rotation and the secular changes can be seen. The colours range linearly from amplitude zero (red) to amplitude 0.6 mmag (blue). The sectors are numbered in the top right corner of each plot. The plots are for 120-s cadence data, unless otherwise noted.

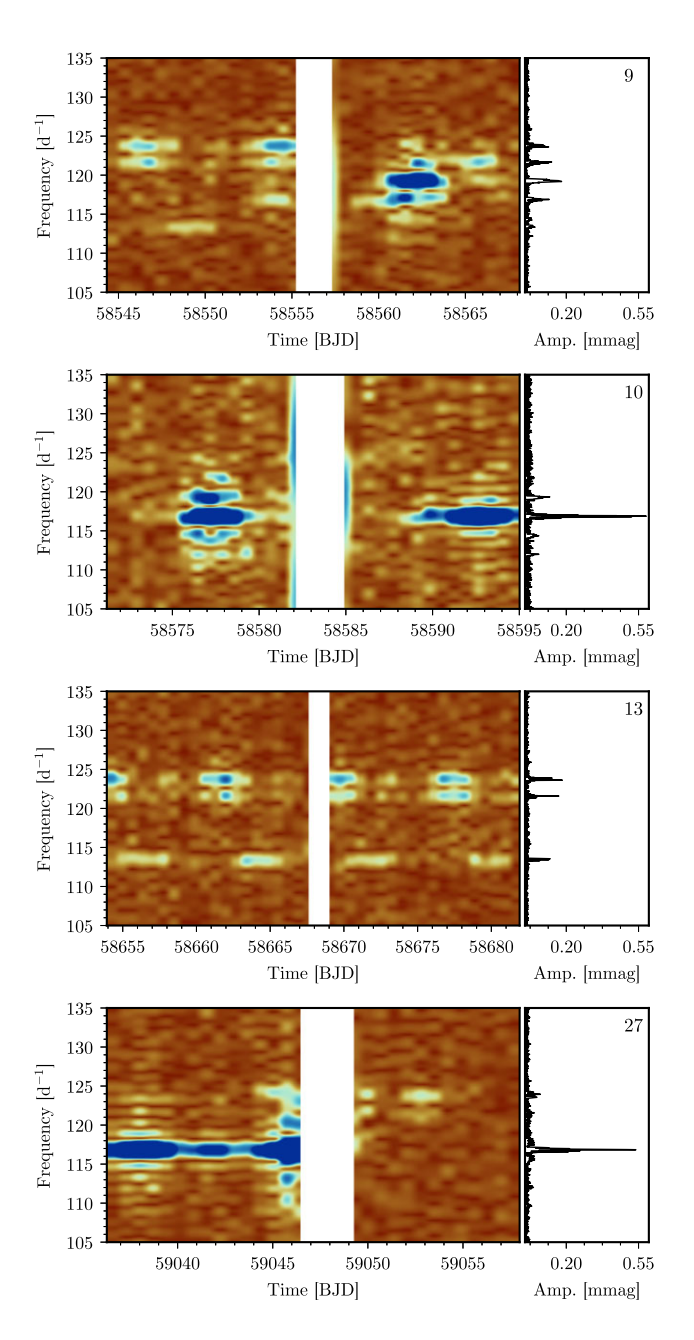


Figure A2. – continued

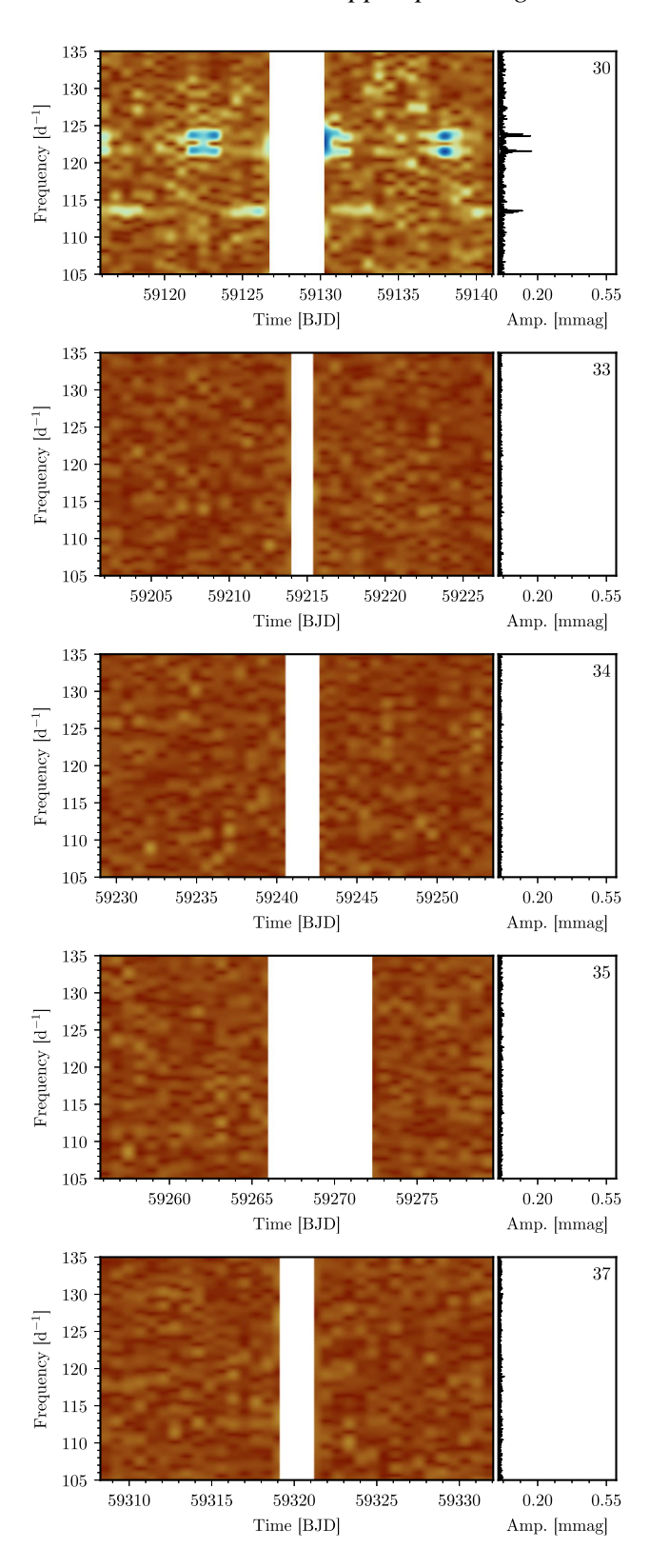


Figure A2. - continued - Wavelets continued. These four sectors are for 200-s cadence data.

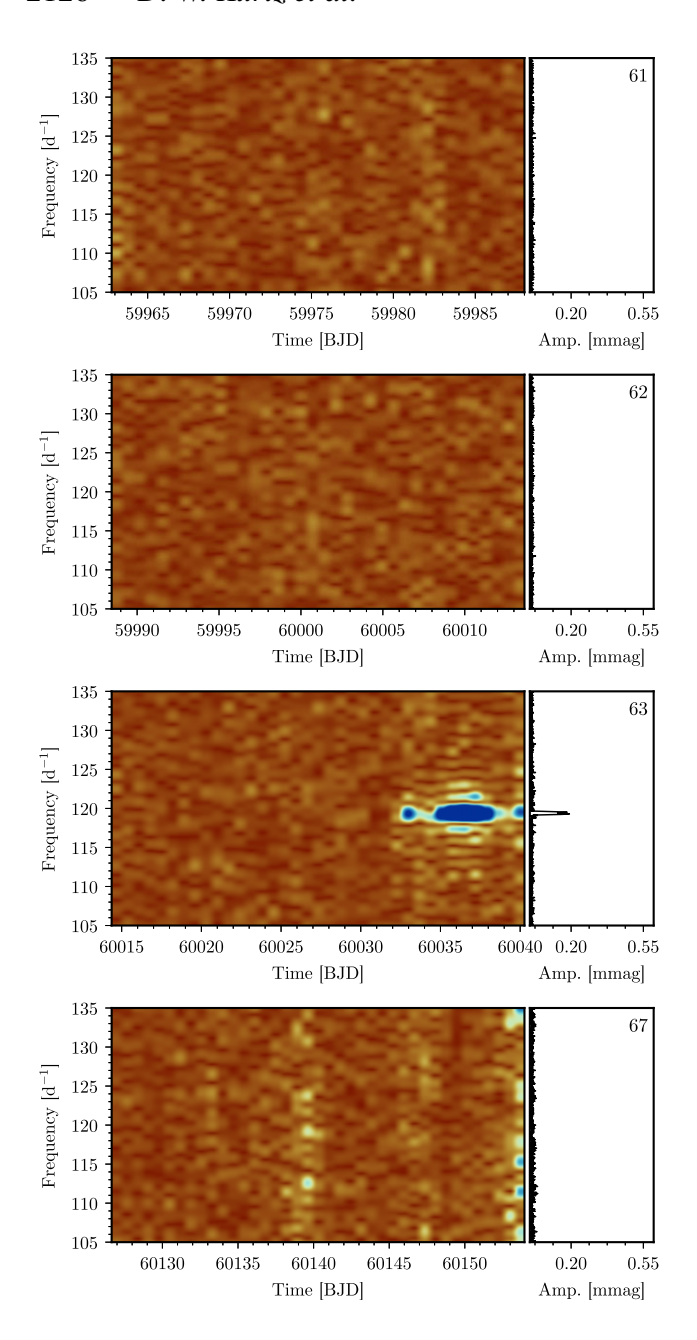


Figure A2. - continued

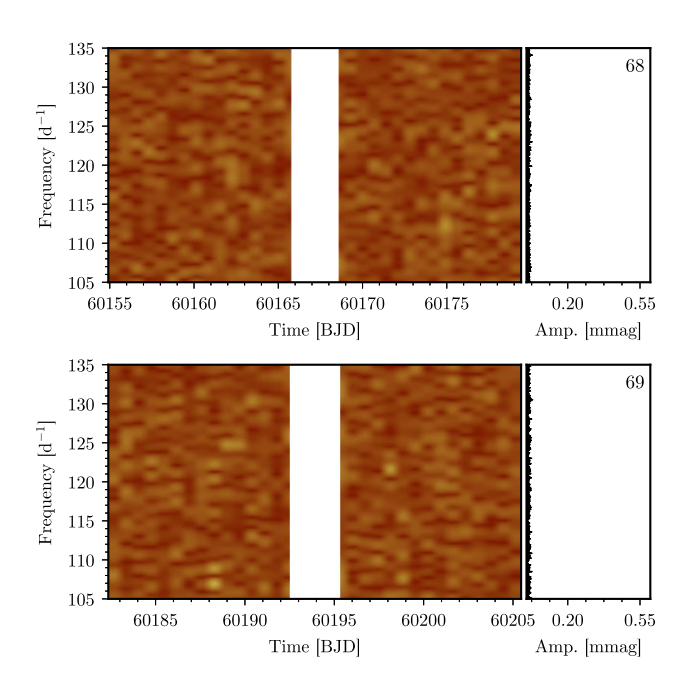


Figure A2. - continued

This paper has been typeset from a T_EX/IAT_EX file prepared by the author.